# Olfactory cortical outputs recruit and shape distinct brain-wide spatiotemporal networks

Teng Ma[1,2,3], Xunda Wang[1,2], Xuehong Lin[1,2], Junjian Wen[1,2], Linshan Xie[1,2], Pek-Lan Khong[4], Peng Cao[3], Ed X. Wu[1,2,5,*] and Alex T. L. Leong[1,2,*]

[1]Laboratory of Biomedical Imaging and Signal Processing, The University of Hong Kong, Pokfulam Hong Kong SAR, China.

[2]Department of Electrical and Electronic Engineering, The University of Hong Kong, Pokfulam Hong Kong SAR, China.

[3]Department of Diagnostic Radiology, Li Ka Shing Faculty of Medicine, The University of Hong Kong, Pokfulam Hong Kong SAR, China.

[4]Department of Diagnostic Radiology and Clinical Imaging Research Center, National University of Singapore, Singapore.

[5]School of Biomedical Sciences, Li Ka Shing Faculty of Medicine, The University of Hong Kong, Pokfulam Hong Kong SAR, China.

[*]Correspondence should be addressed to Alex T. L. Leong, Ph.D. and Ed X. Wu, Ph.D.: Laboratory of Biomedical Imaging and Signal Processing, Department of Electrical and Electronic Engineering, The University of Hong Kong, Pokfulam, Hong Kong, Hong Kong SAR, China.

Fax: +852-2559-8738.

Tel: +852-3917-9713.

Email: tlleong@eee.hku.hk & ewu@eee.hku.hk

**Keywords**

fMRI; Olfactory network; Olfactory Bulb; Anterior Olfactory Nucleus; Piriform Cortex; Brain Connectivity; Optogenetics

## Abstract

Odor information is transmitted from the olfactory bulb to several primary olfactory cortical regions in parallel, including the anterior olfactory nucleus (AON) and piriform cortex (Pir). However, the specific roles of the olfactory bulb and cortical outputs in wider interactions with other interconnected regions throughout the brain remain unclear due to the lack of suitable in vivo techniques. Furthermore, emerging associations between olfactory-related dysfunctions and neurological disorders underscore the need for examining olfactory networks at the systems level. Using optogenetics, fMRI, and computational modeling, we interrogated the spatiotemporal properties of brain-wide neural interactions in olfactory networks. We observed distinct downstream recruitment patterns. Specifically, stimulation of excitatory projection neurons in OB predominantly activates primary olfactory network regions, while stimulation of OB afferents in AON and Pir primarily orthodromically activates hippocampal/striatal and limbic networks, respectively. Temporally, repeated OB or AON stimulation diminishes neural activity propagation brain-wide in contrast to Pir stimulation. Dynamic causal modeling analysis reveals a robust inhibitory effect of AON outputs on striatal and limbic network regions. In addition, experiments in aged rat models show decreased brain-wide activation following OB stimulation, particularly in the primary olfactory and limbic networks. Modeling analysis identifies a dysfunctional AON to Pir connection, indicating the impairment of this primary olfactory cortical circuit that disrupts the downstream long-range propagation. Our study for the first time delineates the spatiotemporal properties of olfactory neural activity propagation in brain-wide networks and uncovers the roles of primary olfactory cortical, AON and Pir, outputs in shaping neural interactions at the systems level.

## Introduction

The olfactory system plays a crucial role in driving behavioral responses that are essential for daily functions. This system facilitates social behaviors by integrating olfactory stimuli with other sensory stimuli and prior experiences[1,2]. Olfactory systems can discriminate among hundreds to thousands of different odorants given the diversity of odorant receptors that specifically bind to the corresponding odorant molecules[3,4]. While olfaction may be more critical for lower-level mammalian species, it remains important for higher primates, as olfactory stimuli can influence emotions, moods, and behaviors[5]. One unique feature of the anatomical organization of the olfactory system is the absence of thalamic processing, indicating that the brain networks pivotal for olfactory processing are distinctly different from other sensory systems. Odor information detected in the olfactory epithelium is first processed at the olfactory bulb (OB), before being routed in parallel to several primary olfactory cortical regions, including the anterior olfactory nucleus (AON) and piriform cortex (Pir). Present studies have primarily examined anatomical projections and targets of local olfactory microcircuits, such as the OB, AON and Pir, including the synaptic interactions between these three connected regions[6-8]. However, the neural interplay between small numbers of anatomically connected regions (i.e., local micro-circuits) is likely insufficient to describe the dynamic properties of information processing that underlie specific brain functions[9-11]. Recent views have advocated for examining and/or modeling polysynaptic interactions across complex networks spanning multiple circuits distributed throughout the brain[11,12]. Moreover, the associations between olfactory-related dysfunctions and neurological disorders such as aging[13], neurodegenerative diseases[14], and recently COVID-19[15-17], highlight the need for examining the olfactory network at the systems level.

Interrogating brain-wide, long-range olfactory networks and their properties require a large-view brain-wide imaging technique that is sensitive to neural activity. However, mapping the brain-wide extent of olfactory regions via traditional functional MRI (fMRI) mapping approaches is technically challenging due to prominent olfactory response habituation[18,19]. Another complicating factor is the need to present a multitude of odors, which affects experimental efficiency and robustness in examining long-range olfactory networks and their properties. Previous attempts to study brain-wide regions involved in olfactory processing in rodents[20,21] and humans[22,23] using task-based fMRI have only identified some known primary olfactory regions, such as the OB, AON, Pir, olfactory tubercle (Tu), and amygdala (Amg). There is a significant gap in the visualization of long-range olfactory networks and the

83 characterization of their functional properties. Notably, the specific roles of the bulbar and AON
84 or Pir cortical outputs in wider interactions with other interconnected regions throughout the
85 brain in olfactory processing remain unclear. In addition, several higher-order regions suspected
86 to mediate more complex olfactory processing remain unidentified and/or to be
87 characterized[5,24,25]. Thus, we designed alternative neuromodulation strategies that can stimulate
88 olfactory-specific neurons in the OB, AON, and Pir with fMRI to characterize brain-wide
89 downstream activation targets and the dynamic properties of long-range olfactory networks.
90 We also aim to employ dynamic causal modeling (DCM)[26], a computational framework that
91 can be used to infer causal interactions among different regions in the olfactory network under
92 different stimulation conditions.

93 In this study, we deployed optogenetic fMRI to achieve reversible, millisecond
94 precision, and cell-type specific stimulation[12,27-31] of excitatory projection neurons in OB (i.e.,
95 mitral and tufted cells), and the olfactory-specific neurons of AON and Pir with computational
96 modeling to investigate the dynamics of large-scale olfactory spatiotemporal networks. Our
97 findings revealed distinct recruitment of downstream targets by olfactory-specific neural
98 populations in AON and Pir. AON-driven neural activities strongly activated hippocampal and
99 striatal networks, while Pir-driven activities preferentially recruited the limbic network.
100 Repeated excitations of AON or OB across multiple fMRI sessions decreased brain-wide
101 activations, while Pir excitations did not alter orthodromic neural activity propagation in long-
102 range olfactory networks. DCM of optogenetic fMRI data showed consistent negative effective
103 connectivity from AON to various downstream targets in the striatal, and limbic networks,
104 indicating a robust inhibitory effect of AON outputs on neural activity propagation in long-
105 range olfactory networks. Further, our systematic examination of long-range olfactory
106 networks in an aged rat model demonstrated an overall decrease in brain-wide activations upon
107 OB excitations, particularly in the primary olfactory and limbic networks. DCM showed that
108 the effective connectivity from AON to Pir switched from positive (healthy) to negative (aged),
109 indicating impairment of this cortical circuit that disrupted neural activity propagation to
110 primary olfactory and limbic networks. This study provides the initial delineation of the
111 spatiotemporal properties of olfactory neural activity propagation in brain-wide networks. We
112 show that primary olfactory cortices (AON and Pir) recruit distinct higher-order brain networks.
113 We also uncover the role of the inhibitory effect of AON and the excitatory effect of Pir outputs
114 in shaping the dynamic properties of neural activity propagation in long-range olfactory
115 networks.

116 # Results

117 **Olfactory bulb and primary olfactory cortices recruit distinct brain-wide long-range**
118 **networks**

119 To identify activated neural networks of the olfactory system, we fused $Ca^{2+}$/calmodulin-
120 dependent protein kinase II alpha (CaMKIIα)-dependent ChR2(H134R) with mCherry to
121 transfect excitatory projection neurons in OB of healthy adult Sprague Dawley rats.
122 Colocalization of mCherry and CaMKIIα confirmed the specific expression of CaMKIIα in
123 mitral and tufted cells within the mitral cell layer and the external plexiform layer of OB (**Fig.**
124 **1A**). Optogenetic stimulation was delivered at 1 Hz (10% duty cycle, 40 $mW/mm^2$), 5, 10, 20
125 and 40 Hz (30% duty cycle, 40 $mW/mm^2$) in a block-design paradigm covering the frequency
126 range of delta (1 Hz, low frequency) to gamma (40 Hz, high frequency) oscillations. Different
127 frequencies were presented in a randomized manner within each fMRI session (**Fig. 1B**).

128 First, we stimulated the OB, the first stage of olfactory information processing in the
129 central nervous system. We detected robust BOLD fMRI activation bilaterally within and
130 beyond primary olfactory networks during 1 Hz stimulation in ipsilateral OB excitatory (**Fig.**
131 **2A**). We identified robust and widespread BOLD responses across both hemispheres in known
132 primary olfactory (AON, Pir, tenia tecta, TT, entorhinal cortex, Ent and olfactory tubercle, Tu),
133 limbic (cingulate, Cg, orbitofrontal, OFC and insular, Ins, cortices, and amygdala, Amg),
134 hippocampal (ventral hippocampus, vHP), striatal (nucleus accumbens, NAc and ventral
135 caudate putamen, vCPu), and sensorimotor (motor, MC, somatosensory, S1, auditory, AC and
136 visual, V1, cortices) regions (**Fig. 2A**). These activations indicate the presence of interactions
137 between the primary olfactory network and other networks associated with high-order
138 functions beyond olfactory processing, such as cognition, reward, and cross-modal sensory
139 processing.

140 Although the first stage of olfactory processing occurs at the OB, primary olfactory
141 cortices (e.g., AON and Pir), which receive parallel direct input from the OB, are also critical
142 for olfaction, as they participate in olfactory memory functions and learning in odor
143 representations within local micro-circuits[32,33] and interactions with the hippocampus[32,34]. As
144 such, we sought to directly examine AON/Pir in our olfactory brain-wide neural networks. We
145 note that direct optogenetic targeting of AON/Pir excitatory neurons may target additional
146 neuronal populations, as not all excitatory neuronal populations in AON and Pir receive
147 olfactory inputs from OB[35,36]. Here, we designed an optogenetic stimulation protocol based on
148 projection targeting (**Supplementary Fig. 1**), whereby the OB afferent terminals were

149 stimulated at AON/Pir, thereby enabling selective stimulation of neurons in AON/Pir that
150 exclusively receive olfactory inputs. Upon 1 Hz stimulation of OB afferents at AON, we
151 observed robust widespread BOLD activations in bilateral primary olfactory, limbic, striatal,
152 sensorimotor cortical and hippocampal regions (**Fig. 2B**), similar to the spatial patterns in our
153 findings for OB stimulation. Meanwhile, 1 Hz optogenetic stimulation of OB afferents at Pir
154 also evoked bilateral BOLD responses in primary olfactory, limbic, and striatal regions albeit
155 with significantly weaker and sparser BOLD activations in bilateral limbic, striatal, and
156 sensorimotor cortical regions (**Fig. 2C**).
157 In addition to the qualitative description of BOLD activation distributions, we further
158 sought to quantify the strength of neural activity at each downstream activation target upon
159 stimulation of the three targets (i.e., OB, AON and Pir). We first calculated the area under the
160 BOLD signal profile (AUC) during the four 20-s 1 Hz optogenetic stimulation blocks for each
161 downstream activation target (**Fig. 2A-C**). However, direct comparisons between AUCs of the
162 three separate optogenetic fMRI experiments are erroneous given the differences in absolute
163 BOLD signal amplitudes, which are likely caused by differences in ChR2 transfection volumes
164 in OB excitatory neurons and OB afferents at AON/Pir, and subsequently the population size
165 of neurons/axonal terminals stimulated. The vast majority of OB neurons are interneurons and
166 not projection neurons that terminate in AON/Pir[37]. Hence, we normalized the AUCs to the
167 sum of BOLD activations of their respective optogenetic fMRI experiments (i.e., defined as
168 BOLD activation strength here; **Fig. 2D**). To distinguish the brain networks that are
169 predominantly recruited by AON- or Pir-driven neural activities compared to OB stimulation,
170 we found that the bulk of OB-driven neural activities were concentrated within the primary
171 olfactory network (i.e., OB, AON, Pir, TT, Ent and Tu; 40.5 ± 1.6 % vs. 27.2 ± 2.7 %, $P < 0.01$
172 for OB vs. Pir; and 40.5 ± 1.6 % vs. 35.6 ± 2.0 %, $P < 0.1$ for OB vs. AON). The strongest
173 BOLD activations within the primary olfactory network (i.e., AON, Pir, TT, Ent, Tu) for OB
174 stimulation experiments aligned with the direct anatomical projections from OB to these
175 targets[37], indicating the successful excitation of OB projection neurons. Interestingly, we
176 discovered that AON-driven activities preferentially recruited the striatal (i.e., NAc and vCPu;
177 13.8 ± 0.6 % vs. 9.8 ± 0.8 %, $P < 0.01$ for AON vs. OB) and hippocampal networks (2.4 ± 0.1 %
178 vs. 1.2 ± 0.2 %, $P < 0.01$ for AON vs. OB), while Pir-driven activities strongly targeted the
179 limbic network (i.e., Cg, PrL, OFC, Ins and Amg; 39.5 ± 2.8 % vs. 30.3 ± 1.4 %, $P < 0.05$ for
180 Pir vs. OB). Meanwhile, all three stimulated regions showed relatively equal recruitment of
181 sensorimotor networks. The specificity afforded by perturbing the OB afferents at AON and
182 Pir indicated that these olfactory inputs recruit distinct downstream targets in primary olfactory,

183 limbic, hippocampal and striatal networks, despite sharing extensive overlaps in anatomical
184 projections[25,37-39].
185 We also examined BOLD activations upon optogenetic stimulation of the three primary
186 olfactory regions (i.e., OB, AON and Pir) at various frequencies. We observed robust bilateral
187 activations during 5 Hz stimulation of OB excitatory neurons (**Supplementary Fig. 2A**) and
188 OB afferents in AON (**Supplementary Fig. 3A**), although the activations at the contralateral
189 hemisphere were relatively weaker. The subsequent increase in stimulation frequencies to 10
190 Hz, 20 Hz and 40 Hz resulted in robust activations that were predominantly localized in the
191 ipsilateral primary olfactory and limbic networks (**Supplementary Figs. 2B-D & 3B-D**).
192 Meanwhile, BOLD activations were only detected in ipsilateral primary olfactory, limbic, and
193 striatal networks when higher frequency optogenetic stimulation was presented to OB afferents
194 at Pir (**Supplementary Fig. 4**). To examine long-range olfactory networks, we focused on the
195 1 Hz optogenetic stimulation experiments.
196 Altogether, our approach to stimulating the three primary olfactory regions (i.e., OB,
197 AON and Pir) provides valuable insights into the networks that are pivotal for olfactory
198 processing. Notably, the distinction in brain networks that are recruited by olfactory-specific
199 neural populations in AON vs. Pir such as hippocampal and striatal vs. limbic reveal functional
200 insight into the AON and Pir in olfactory processing.
201
202 **AON and Pir circuit outputs shape the dynamic properties of long-range olfactory**
203 **networks**
204 The distinct spatiotemporal propagation properties and the recruitment of different long-range
205 olfactory-related networks suggest varied modulatory roles for OB, AON and Pir when
206 interacting with their downstream targets. Here, we first examined the dynamics of BOLD
207 activations across multiple 1 Hz stimulation sessions. We observed distinct changes to the
208 spatiotemporal properties of BOLD fMRI activations across the three optogenetic fMRI
209 sessions. Overall, the brain-wide activations at primary olfactory, limbic, striatal, and
210 sensorimotor cortical networks in our first fMRI session showed an appreciable decreasing
211 trend in subsequent stimulation sessions. For OB 1 Hz stimulation in the 2$^{nd}$ fMRI session,
212 there was a decrease in the BOLD activations at most of the downstream targets across multiple
213 networks. These include the ipsilateral OB (i.e., the stimulation site), contralateral TT, and
214 bilateral AON, Pir, Ent and Tu of the primary olfactory network; bilateral OFC, Ins and Amg
215 of the limbic network; bilateral NAc and ipsilateral vCPu of the striatal network; and bilateral
216 MC and ipsilateral AC of the sensorimotor network (**Fig. 3A** and **Supplementary Fig. 5A**).

217 BOLD activations during the 3rd fMRI session also showed decreased activations (i.e., 3rd vs
218 1st fMRI session; **Fig. 3A** and **Supplementary Fig. 5A**). Comparatively, we observed a
219 dramatic decrease in activations upon 1 Hz stimulation of OB afferents at AON during the later
220 fMRI sessions. We found diminished or even absent bilateral activations in downstream targets.
221 Specifically, activations evoked by AON stimulation showed a significant decrease in the 2nd
222 and 3rd sessions at all regions except contralateral OB (**Fig. 3B** and **Supplementary Fig. 5B**).
223 Notably, activations at bilateral vHP also significantly decreased despite having the weakest
224 activation among downstream targets during the 1st fMRI session. However, the activations
225 upon 1 Hz stimulation of OB afferent inputs at Pir remained relatively stable across fMRI
226 sessions in the primary olfactory, limbic, striatal and sensory cortical networks except for a
227 slight decrease in Amg (**Fig. 3C** and **Supplementary Fig. 5C**).
228 We then sought to identify the driver of these distinct influences of OB, AON and Pir
229 stimulation on the dynamic response properties of long-range olfactory-related networks.
230 Conventional analyses of BOLD fMRI data such as general linear model (GLM) and
231 comparisons of the energy of BOLD signal profiles are insufficient and unable to infer the
232 causal influences of OB-, AON- and Pir-driven neural activity on their downstream targets.
233 Here, we applied DCM[26] on our optogenetic fMRI data to parametrize the downstream effects
234 on selected targets in the right brain hemisphere (i.e., the same hemispheric side to the
235 optogenetic stimulation site). Specifically, we used DCM to computationally model the
236 effective connectivity strength of selected downstream connections in OB, AON and Pir
237 stimulation data. We defined a six-node brain network and its connections that encompassed
238 regions from primary olfactory (OB, AON, Pir and Ent), striatal (vCPu) and limbic (Amg)
239 networks (**Fig. 4A**). These connections were primarily based on the well-defined anatomical
240 feedforward and feedback projections involving the three major primary olfactory regions (i.e.,
241 OB, AON and Pir). For simplicity, we did not model other downstream regions to avoid data
242 overfitting issues[40]. Further, we only modeled the optogenetic fMRI data from the 1st session,
243 because BOLD signal profiles for the 2nd and 3rd fMRI sessions had lower SNR due to
244 decreased and in some cases absent activations in long-range olfactory networks. Overall, we
245 observed that the connectivities were primarily positive (i.e., excitatory effects) between the
246 nodes in the primary olfactory network (i.e., OB, AON and Pir; **Fig. 4B**) for all three different
247 stimulations, corroborating documented reciprocal glutamatergic excitatory projections
248 between these three regions[25,38,41,42]. Notably, we observed a significant negative AON and
249 positive Pir connectivity to downstream targets (i.e., Ent, vCPu and Amg; **Fig. 4B**).
250 Quantitative comparisons of the effective connectivity strengths from AON/Pir to Ent, vCPu

251 and Amg confirmed the robust negative AON vs. positive Pir connectivity to downstream
252 targets (*AON-Ent vs. Pir-Ent*: -0.21 ± 0.14 vs. 0.39 ± 0.08 Hz, $P < 0.05$ for OB stimulation and
253 -0.34 ± 0.09 vs. 0.35 ± 0.06 Hz, $P < 0.01$ for AON stimulation; *AON-vCPu vs. Pir-vCPu*: -0.03
254 ± 0.06 vs. 0.31 ± 0.10 Hz, $P = 0.053$ for OB stimulation, -0.37 ± 0.08 vs. 0.40 ± 0.06 Hz, $P <$
255 0.01 for AON stimulation and -0.14 ± 0.06 vs. 0.28 ± 0.07 Hz, $P < 0.05$ for Pir stimulation;
256 *AON-Amg vs. Pir-Amg*: -0.10 ± 0.10 vs. 0.26 ± 0.04 Hz, $P < 0.05$ for OB stimulation, -0.25 ±
257 0.12 vs. 0.33 ± 0.06 Hz, $P < 0.05$ for AON stimulation and -0.16 ± 0.06 vs 0.30 ± 0.06 Hz, $P$
258 $< 0.05$ for Pir stimulation; **Fig. 4C**). These results demonstrate distinct inhibitory effect of
259 AON and excitatory effect of Pir outputs in long-range olfactory networks. We speculate that
260 the significant decrease in BOLD activations during repeated OB or AON stimulations, but not
261 during Pir stimulations, arises from the strong inhibitory effect of AON outputs to various
262 targets beyond the local olfactory microcircuits (i.e., OB, AON and Pir). Taken together, our
263 results indicate that the outputs of primary olfactory cortices, AON and Pir, shape the dynamic
264 properties of neural activity propagation in long-range olfactory networks.
265
266 **Repeated AON stimulations diminish orthodromic neural activity propagation**
267 We recognize that our optogenetic stimulation protocols, particularly the stimulations of ChR2-
268 transfected OB afferents at AON and Pir compared to the stimulation of OB excitatory neurons
269 (**Supplementary Fig. 1**), can be sensitive to antidromic-driven neural activities due to
270 activation of the axon terminals instead of the soma[43,44]. To verify the neural activities
271 underlying our fMRI findings and delineate features of neural activity propagation, we
272 conducted local field potential (LFP) recordings at seven regions in the right brain hemisphere.
273 These regions include the ipsilateral OB, AON, Pir, vCPu, V1, Amg, vHP and dHP. The
274 stimulation paradigm (i.e., block-designed and three recording sessions for each animal)
275 matches that from the fMRI experiments. The averaged four 60-s-block LFP traces (**Fig. 5A-**
276 **C**) and the subsequent power analysis of these LFP traces for the first recording session (**Fig.**
277 **6A-C**) largely concurred with the magnitude and temporal profiles of BOLD fMRI activations
278 (**Fig. 2A-C**), with evoked LFPs observed in all recorded regions during the first experimental
279 session. Parallel to our fMRI findings, the strength of neural activities, which were quantified
280 through LFP power analysis (i.e., area under absolute LFP trace normalized to 30-s baseline
281 LFP power), was also decreased during repetitive 1 Hz stimulation of OB or OB afferents at
282 AON but was relatively unchanged under Pir stimulation (1$^{st}$ vs 2$^{nd}$ and 3$^{rd}$ recording sessions;
283 **Fig. 6**).

284 We next characterized the latency of neural activity at each recorded region by using
285 the first appreciable evoked LFP peak to represent the initial neuronal population activity[28,29,45]
286 (**Fig. 5**). Negative LFP peaks occurred first in each of the three stimulation targets, while
287 positive peaks were observed for their corresponding downstream targets. During somatic
288 activation of ipsilateral OB excitatory neurons, there is an evoked LFP response latency of 6.1
289 ± 0.7 ms (**Fig. 5A**), which is within the 5-6 ms range documented for response latency of OB
290 excitatory neurons in the presence of natural odors[46,47]. We measured delays of 8.7 ± 0.9 ms
291 and 8.2 ± 1.0 ms between OB and AON, and OB and Pir, respectively, consistent with the
292 reported 5-10 ms neural activity propagation along monosynaptic projections of OB to AON[48]
293 and Pir[49-51]. Neural activities from ipsilateral OB arrived at ipsilateral vCPu and V1 in 9.7 ±
294 2.6 ms and 11.7 ± 3.0 ms in line with the axonal conduction speed between OB and
295 striatal[52,53]/sensorimotor cortical[54,55] regions. Lastly, the long delays of 37.9 ± 0.9 ms and 39.2
296 ± 2.1 ms from ipsilateral OB to vHP and dHP respectively, indicate that neural activities
297 propagated through polysynaptic projections of OB-primary olfactory cortices-Ent-HP[51,56].
298 When stimulating the OB afferents in AON, we found a response latency of 7.7 ± 0.7 ms locally
299 at AON (**Fig. 5B**). A subsequent delay of 7.2 ± 1.8 ms and 5.0 ± 0.9 ms was then measured
300 between AON and its downstream targets in the primary olfactory network (i.e., OB and Pir),
301 corroborating reported values of 4-10 ms[57]. The presence of a significant delay between AON
302 and OB neuronal population activities with appreciable jitter demonstrates that neural activity
303 propagation through the activation of OB axonal terminals at AON is largely orthodromic in
304 our experiment. Neural activity from olfactory-specific AON neurons also propagated in an
305 orthodromic manner to targets in the striatal (vCPu), sensorimotor cortical (V1) and limbic
306 (Amg) networks, 7.1 ± 1.0 ms, 7.5 ± 1.6 ms, and 7.0 ± 0.4 ms, respectively, in line with axonal
307 conduction speed[58]. Meanwhile, excitation of the OB afferents at Pir evoked a response latency
308 of 5.9 ± 0.6 ms (**Fig. 5C**), which closely matched the latency of ~5 ms upon optogenetic
309 stimulation of afferents to Pir in a previous study[41]. Subsequently, the neural activity
310 propagated from Pir to OB, AON, vCPu, V1, and Amg at a delay of 8.1 ± 0.5 ms, 8.2 ± 0.3 ms,
311 7.9 ± 0.8 ms, 8.6 ± 0.5 ms, and 8.9 ± 0.8 ms, respectively. We conclude that the observed
312 neural activity propagation is predominantly orthodromic given the significant delay and jitter
313 of excitatory inputs from Pir to OB. Notably, the neural activity propagated in 28.2 ± 3.0 ms
314 from Pir to vHP, while the propagation speed from the AON to vHP was faster at 22.2 ± 1.7
315 ms. The longer delay between Pir and the hippocampus suggests the presence of an
316 intermediary region between the Pir and Ent.

317 Taken together, our electrophysiological recordings showed the direct involvement of
318 both local and long-range projections that mediate the propagation of neural activity in
319 olfactory networks. Moreover, orthodromic propagations when stimulating OB afferents at
320 AON and Pir indicate that the long-range inhibitory effect of AON and excitatory effect of Pir
321 outputs, which shaped the dynamic properties of BOLD activations in olfactory networks, are
322 predominantly driven by the feedforward projections of olfactory-specific neurons in the
323 primary olfactory cortices.
324
325 **Long-range olfactory networks of aged brains exhibit decreased neural activations and**
326 **impaired AON to Pir connectivity**
327 Informed by the insights gained from characterizing the spatiotemporal properties of long-
328 range olfactory networks in normal healthy brains, we deployed our optogenetic fMRI platform
329 to examine the systemic dysfunction of olfactory networks in a diseased brain. Here, we
330 employed a D-galactose model of accelerated aging in rodents. This model induces higher
331 levels of oxidative stress, mitochondrial dysfunction, and cellular apoptosis. These factors can
332 lead to the decline of cognitive functions, which is a key symptomatic hallmark of age-related
333 brain senescence[59,60]. Spatially, we observed that 1 Hz stimulation of the OB excitatory neurons
334 evoked bilateral activations in all brain regions like primary olfactory, limbic, hippocampal,
335 striatal and sensorimotor networks (**Fig. 7A** vs. **Fig. 2A**). These spatially preserved activations
336 indicate that neural activity propagation in long-range olfactory networks remains intact in
337 aged brains. However, the strength of neural activities at downstream activation targets
338 exhibited a general decrease in both brain hemispheres when compared to healthy animals. A
339 significant decline in BOLD activations was mostly identified in ipsilateral primary olfactory
340 (aged vs. healthy; AONR: 16.4 ± 3.8 vs. 33.4 ± 6.5, $P < 0.05$; PirR: 33.5 ± 6.0 vs. 58.0 ± 8.4,
341 $P < 0.05$; TTR: 15.1 ± 4.8 vs. 41.3 ± 7.0, $P < 0.01$) and ipsilateral limbic networks (CgR: 7.6
342 ± 1.9 vs. 15.5 ± 1.9, $P < 0.01$; OFCR: 19.4 ± 3.0 vs. 36.7 ± 3.8, $P < 0.01$; InsR: 29.2 ± 3.8 vs.
343 40.6 ± 5.0, $P < 0.05$). We also observed a general trend of decline in the other regions of the
344 primary olfactory network (PirL: 23.7 ± 5.4 vs. 37.8 ± 7.1, $P = 0.07$ and EntR: 26.0 ± 4.8 vs.
345 38.3 ± 5.7, P = 0.06), and the ipsilateral sensorimotor network (MCR: 16.5 ± 2.4 vs. 24.5 ± 4.3,
346 $P = 0.059$). Surprisingly, there was a general trend of increased BOLD activations in the striatal
347 network (NAcR: 27.7 ± 2.8 vs. 20.3 ± 3.2, $P = 0.055$). DCM of the optogenetic fMRI data in
348 aged animals revealed a switch in the effect of ipsilateral AON outputs to ipsilateral Pir from
349 excitatory to inhibitory (healthy vs. aged; 0.23 ± 0.09 vs. -0.12 ± 0.10 Hz, $P < 0.05$), indicating
350 dysfunction of a key primary olfactory cortical circuit in the olfactory network disrupting

351 neural activity propagation to primary olfactory and limbic networks. Note, that in healthy
352 animals (**Fig. 2D**), the primary olfactory network was preferentially recruited by AON-driven
353 neural activities, while the limbic network was recruited mainly by Pir-driven neural activities.
354 The predominant effect observed in the right hemisphere was likely due to the stimulation of
355 the right/ipsilateral OB. We expect both hemispheres to be affected equally in aged brains.
356

357 ## Discussion

358 As a major sensory system, the olfactory system has been linked to numerous non-olfactory
359 regions pivotal for sensory perception and higher-order cognition[5], yet recent views highlight
360 the significant gap in understanding where and how olfactory information is distributed
361 downstream beyond these known primary regions[5,61-64]. In this study, we deployed optogenetic
362 stimulation, fMRI, and electrophysiological recordings to systematically dissect the
363 spatiotemporal properties of long-range olfactory networks. We discovered that olfactory-
364 specific neural populations in AON and Pir distinctly recruited downstream targets such as the
365 hippocampal and striatal networks for AON-driven neural activities, and the limbic network
366 for Pir-driven neural activities. Further analysis revealed robust adaptation of brain-wide
367 BOLD fMRI activations upon repeated optogenetic stimulations of OB afferents in AON or
368 OB excitatory neurons, which were absent when stimulating OB afferents at Pir.
369 Computational modeling of our optogenetic fMRI data through DCM indicated a significant
370 inhibitory effect of AON outputs to downstream targets in the olfactory network compared to
371 the excitatory effect from Pir outputs. These results highlight a likely dominant role of
372 olfactory-specific AON neural populations in mediating sensory adaptation in the presence of
373 olfactory inputs. Electrophysiological recordings demonstrated predominant orthodromic
374 neural activity propagation to downstream targets in long-range olfactory networks for all
375 optogenetic stimulations and verified the adaptation of optogenetically-evoked neural activities
376 observed in the fMRI experiments. In addition, our systematic comparisons of the olfactory
377 networks between aged and healthy brains revealed an overall decrease in the amplitudes of
378 BOLD activations, particularly in regions of the primary olfactory and limbic networks, along
379 with increased inhibitory effect of AON outputs to the Pir, indicating impairment of this key
380 olfactory cortical circuit. Our optogenetic fMRI approach constitutes the initial
381 characterization of 1) the spatiotemporal properties of long-range olfactory networks and 2)
382 the roles of AON and Pir outputs in shaping the dynamic properties of olfactory neural activity
383 propagation in healthy and diseased brains.

384 Habituation or adaptation shows decreased responses to repeated or continuous
385 stimuli[65,66]. Olfactory adaptation refers to the ability of the network to adjust its sensitivity at
386 different stimulus intensities, which is essential for retaining high sensitivity to odd/another
387 stimulus under repetitive or prolonged odor stimulation[67]. This fundamental property of all
388 sensory systems prevents overstimulation and retains alertness to the environment[66]. Olfactory
389 adaption occurs at two levels: peripheral – at the level of olfactory receptors – and central – at
390 the level of the central nervous system[66]. At present, the underlying neural mechanism of
391 peripheral adaptation that occurs at the molecular level[67], and central adaptation within the
392 primary olfactory local network (i.e., OB[68,69], AON[25], Pir[70,71] and Tu[72]) has been shown to
393 require glutamate release in the OB[73]. However, the significant decreases in BOLD activation
394 across all downstream targets indicate that olfactory adaptation may occur more broadly across
395 various targets of the olfactory network rather than being localized at the OB. Specifically, our
396 results reveal a previously undefined role of the AON in mediating olfactory adaptation at the
397 systems level, as we showed strong adaptation of optogenetically-evoked neural activities (**Figs.**
398 **3B** and **6B**) upon 1 Hz stimulation of OB projection neurons and OB afferent inputs at AON,
399 but not OB afferents at Pir, along with robust inhibitory effects of AON outputs to Ent, vCPu
400 and Amg (**Fig. 4C**).
401 AON sends robust centrifugal inputs to OB that can inhibit bulbar outputs[25,57] and
402 robust glutamatergic feedforward projections that bilaterally innervate the Pir[41,74], to enhance
403 activation of piriform neurons in response to odor[41]. Further, recent studies on AON functions
404 revealed its involvement in interhemispheric communication[25,75,76], sensory gating[77,78] and
405 odor memory[32,35], indicating a predominant role of AON as a hub to process olfactory
406 information (i.e., odor identity decoding and gain control of OB outputs[42]). In our study, only
407 stimulation of the ipsilateral AON evoked bilateral brain-wide BOLD responses in primary
408 olfactory (i.e., Pir, Tu), limbic (i.e., Ins, OFC) and striatal regions (i.e., NAc, vCPu) at all
409 frequencies (**Fig. 2B and Supplementary Fig. 2**), indicating the pivotal role of AON in
410 olfactory processing between both hemispheres. AON receives centrifugal projections from
411 HP, which represents its ability to process odor memory-related contextual
412 information[32,35,77,79,80]. Notably, our fMRI analysis also showed that AON-driven neural
413 activities preferentially recruited the hippocampal network. Further, we observed robust
414 bilateral brain-wide activations initiated by 1 Hz stimulation at AON during the first fMRI
415 session, which were followed by dramatically decreased downstream activations under
416 repetitive stimulations (**Fig. 3**). We speculate that AON exerts robust feedforward neural
417 activity propagation to long-range downstream targets after the early stage of olfactory

418 processing at OB. However, in the presence of repeated strong activations of olfactory-specific
419 neural populations in AON (i.e., through OB or AON stimulations), centrifugal feedback from
420 the AON, which preferentially controls the gain of OB neuronal responses[42], likely inhibited
421 OB outputs[25,57], resulting in decreased brain-wide activations in later fMRI sessions. Further,
422 we identified robust inhibitory AON outputs to non-primary olfactory brain regions (i.e., Ent,
423 vCPu, Amg; **Fig. 4C**), regardless of the stimulated region, indicating that neural adaptation
424 processes could also be distributed beyond local olfactory micro-circuits (i.e., centrifugal AON
425 outputs to OB). We note that olfactory adaptation at the systems level is quite under-studied,
426 and future studies may examine the circuit properties at these long-range targets when
427 processing odor information.

428 Pir sends ipsilateral inputs to OB and AON[39,81] and functions to amplify the inhibition
429 of odor-related signals and finely tune them in OB[42,82], in order to process and identify critical
430 features of an odor. Although, studies have noted a significant overlap in the functions of Pir
431 during olfactory processing with those of AON[37,83,84], the recurrent neural architecture of
432 Pir[85,86] stands in contrast to that of AON. These structural differences indicate how Pir
433 processes olfactory inputs from OB distinctly. We found that Pir-driven neural activities
434 preferentially recruited regions in the limbic network, which differed from those primarily
435 recruited by AON. Anatomically, Pir projects extensively to regions of the limbic network such
436 as OFC and Amg[87,88], which demonstrates the specificity in our optogenetic fMRI approach
437 when dissecting the spatiotemporal properties of long-range olfactory networks. Overall, we
438 also observed that exciting olfactory-specific neurons in Pir produced weaker brain-wide
439 BOLD activations than OB or AON stimulation (**Fig. 2C** and **Supplementary Fig. 4**). We
440 posit this occurs from the recurrent neural architecture of Pir (i.e., dense reciprocal synaptic
441 connections between olfactory-specific neurons in Pir and inhibitory interneurons), which can
442 recruit sustained inhibition that subsequently diminishes overall Pir cortical neural activity in
443 the presence of olfactory inputs[85].

444 The ability to detect and discriminate odors declines during aging, leading to a decrease
445 in quality of life and diminished appetite with a concomitant impact on nutrition[89]. Decreased
446 olfactory function with aging parallels generalized age-related deficits in sensory functions and
447 cognition that occur in the absence of obvious disease states[14]. However, studies in rodents
448 demonstrate that the decreased ability to perceive odors was not associated with a general
449 decline in the number of receptors/cells in the olfactory epithelium or a decline in neuronal
450 populations (i.e., mitral and tufted cells, and interneurons) in the OB[13]. Instead, the synaptic
451 density in the glomeruli of the OB appears diminished[13], suggesting impaired downstream

452 olfactory information processing from the OB to targets in the cortical and subcortical regions.
453 At present, there is no consensus on the most representative animal model of aging that best
454 mimics the human condition. D-galactose has been shown to induce advanced glycation end
455 products formation, a process that contributes to early phases of age-related diseases in both
456 humans and rodents[90,91]. With the discovery of diminished brain-wide neural activity
457 propagation, our results in a D-galactose rat model indicate that the impairment of OB
458 downstream olfactory information processing is likely true in aged brains. We also found the
459 switch from positive effective connectivity of AON to Pir and AON to vCPu in healthy animals
460 to significantly negative ones in aged animals, indicating abnormal AON output to downstream
461 targets in long-range olfactory networks during olfactory information processing. Notably, age-
462 related neurodegenerative diseases (e.g., Alzheimer's and Parkinson's disease) can exhibit
463 olfactory impairments in the early stages with cell loss and axonal degradation in AON[92-94].

464 In summary, our study demonstrates the distinct recruitment of higher-order brain
465 networks by primary olfactory cortices (AON and Pir), including the identification of AON
466 and Pir outputs that can shape the dynamic properties of neural activity propagation in long-
467 range olfactory networks in healthy and aged brains. Such documentation of long-range
468 olfactory networks and their properties will be of great value to both neuroscientists and
469 clinicians. By gaining an integrated understanding of olfactory networks and their fundamental
470 properties in both healthy and aged brains, we can develop therapeutic strategies for
471 neurological diseases associated with olfactory system dysfunctions.

472 ## Methods

473 **Animal subjects.** Adult male Sprague Dawley rats were used in all experiments. Animals were
474 individually housed under a 12-h light/dark cycle with access to food and water ad libitum. All
475 animal experiments were approved by the Committee on the Use of Live Animals in Teaching
476 and Research (CULATR) of the University of Hong Kong. Seven groups of animals were used:
477 Group I ( n = 11) for optogenetic fMRI experiments upon olfactory bulb (OB) stimulation;
478 Group II (n = 11) for optogenetic fMRI experiments upon anterior olfactory nucleus (AON)
479 stimulation; Group III (n = 9) for optogenetic fMRI experiments upon piriform cortex (Pir)
480 stimulation; Group IV (n = 7) for electrophysiological recordings upon OB optogenetic
481 stimulation; Group V (n = 7) for electrophysiological recordings upon AON optogenetic
482 stimulation; and Group VI (n = 5) for electrophysiological recordings upon Pir optogenetic
483 stimulation; and Group VII (n = 13) for optogenetic fMRI experiments upon OB stimulation
484 in aged rats.

485 Note that for the electrophysiological experiments, not all animals resulted in successful
486 recordings in all electrode locations. For Group IV, only OB, AON, Pir, vCPu and V1 were
487 recorded in all 7 animals, whereas only 2/7 in vHP and 3/7 animals in dHP. For Group V, AON
488 in 7 animals, OB in 6 animals, whereas only 5/7 in Pir, 3/7 in vCPu, V1 and vHP, and 4/7
489 animals in Amg. For Group VI, OB, Pir and vHP in 5 animals, followed by 4/5 in AON, 3/5 in
490 vCPu and V1, and 2/5 animals in Amg.

491 **Virus packaging.** Recombinant AAV vectors were serotyped with AAV5-coated proteins and
492 produced by the Vector Core of the University of North Carolina. Viral titer in particles/mL
493 was $4 \times 10^{12}$ for AAV5CaMKII $\alpha$-ChR2(H134R)-mCherry. Maps are available online from
494 http://www.stanford.edu/group/dlab/optogenetics.

495 **Accelerated aging animal model induction protocol.** D-galactose (50 mg/kg, subcutaneous)
496 was administered daily to 10-week-old male adult SD rats for a total duration of 8 weeks. D-
497 galactose administration in rodents has been shown to cause increased oxidative stress,
498 mitochondrial dysfunction and cellular apoptosis, which leads to the deterioration of cognitive
499 functions, a primary symptomatic hallmark of senescence of the brain[59,60].

500 **Stereotactic surgery for viral injection.** Stereotactic surgeries were performed with rats at 6-
501 7 weeks of age for group I to VI, and at 15 weeks (i.e., 5 weeks in on the daily D-galactose
502 administration) for group VII. Rats were anesthetized with an intraperitoneal bolus injection of
503 a ketamine (90 mg/kg) and xylazine (40 mg/kg) mixture. After shaving the scalp, rats were

504 secured in a stereotactic apparatus with non-rupturing ear bars and craniotomy was conducted.
505 Buprenorphine (0.05 mg/kg, subcutaneous) was administered to minimize pain. A heating pad
506 was used to prevent hypothermia. Viral injection was performed at two depths in OB (+7.5 mm
507 anterior to Bregma, +1.8 mm medial-lateral right hemisphere, -1.8 mm and -2.1 mm from the
508 surface of dura), with subsequent verification by high-resolution anatomic MRI. Viral
509 constructs were delivered at 1.5 μL volume at each depth through a 5 μL syringe and 33-gauge
510 beveled needle injected at a rate of 150 nL/min. The injection needle was held in place for 10
511 min and retracted from the brain slowly. Scalp incision was sutured, and animals were kept on
512 a heating pad until recovery from anesthesia. Buprenorphine (0.05 mg/kg, subcutaneous) was
513 administered post-injection twice daily for 72 hours to minimize discomfort. Enrofloxacin was
514 also administered orally for 72 hours to minimize infection and inflammation post-surgery.
515 Animals recovered for 4-5 weeks before conducting MRI and electrophysiology experiments.

516 **Animal preparation for optogenetic fMRI experiments.** Before surgery, animals were
517 anesthetized with isoflurane (induction 3% and maintenance 2%) and secured on a stereotactic
518 frame. Before animals were placed in-magnet, surgery was performed under 1.2-2.0%
519 isoflurane to implant a custom-made plastic optical fiber cannula (core diameter = 450 μm,
520 outer diameter = 500 μm). Implantation of the cannula was made at three different locations in
521 the ipsilateral/right brain hemisphere depending on the experiments, namely at OB (+7.5 mm
522 anterior to Bregma, +1.8 mm medial-lateral, -2.1 mm from the surface of dura), AON (+5.2
523 mm anterior to Bregma, +1.8 mm medial-lateral, -4.3 mm from the surface of dura) and Pir
524 (+4.2 mm anterior to Bregma, +3.1 mm medial-lateral right hemisphere, -5.4 mm from the
525 surface of dura). Following a midline incision, a craniotomy was performed at these located
526 coordinates. The fiber tip was scored to create a beveled edge to facilitate insertion of the fiber
527 and minimize injury to brain tissue. The fiber cannula was then made opaque using heat
528 shrinkable sleeves to prevent light leakage during stimulation and the eyes of the animals were
529 blindfolded to prevent undesired visual stimulation, as in our previous studies[28-31,45,95]. Dental
530 cement was applied to the fiber cannula to affix it to the skull. The optical fiber tip was typically
531 situated in the mitral cell layer and external plexiform layer in OB stimulation experiments,
532 dorsal pars principalis of the AON to target OB afferents at AON, and anterior Pir for OB
533 afferents at Pir with verification by high-resolution anatomical MRI (**Fig. 1A**). The spatial
534 spread from the fiber tip for 473 nm blue light is rather small (200 μm and 350 μm at 50% and
535 10% of initial light intensity, respectively) and has little or no in the backward and lateral
536 directions[28,96], confining the optogenetic stimulation to the excitatory neurons in OB, and the

537 axonal terminals of OB at AON and Pir, respectively. Buprenorphine (0.05 mg/kg,
538 subcutaneous) was administered post-implantation.

539 The animals were mechanically ventilated at a rate of 60 breaths per minute with 1.0%
540 isoflurane in room-temperature air using a ventilator (TOPO, Kent Scientific, Torrington, CT).
541 One drop of 2% lidocaine was applied to the chords to minimize discomfort before
542 endotracheal intubation. During all fMRI experiments, animals were placed on a plastic holder,
543 and their heads were fixed with a tooth bar and plastic ear bars with screws. Continuous
544 physiological monitoring was performed using sensors from an MRI-compatible system (SA
545 Instruments, Stony Brook, NY). Rectal temperature was maintained at ~37.0 °C using a water
546 circulation system. Vital signs were within normal physiological ranges (rectal temperature:
547 36.5-37.5 °C, heart rate: 350-420 beats/min, breathing: ~60 breaths/min but not synchronized
548 to optogenetic stimulation, oxygen saturation level: >95%) throughout the experiments.

549 **MRI scanner-synchronized optogenetic stimulation.** An Arduino programming board
550 synchronized the scanner trigger and the lasers for optogenetic stimulation. Computers and
551 light delivery systems were kept outside the magnet, and optical patch cables (5-10 m)
552 delivered light into the bore of the scanner. For optogenetic stimulation, blue light was
553 delivered using a 473 nm Diode-pumped solid-state laser, measured before scanning as 8 mW
554 at the fiber-tip (450 μm, NA = 0.5) corresponding to a light intensity of 40 mW/mm$^2$. For all
555 fMRI experiments (i.e., OB, AON or Pir stimulation), five frequencies were used (1 Hz with a
556 10% duty cycle; 5, 10, 20 and 40 Hz with a 30% duty cycle). OB, AON or Pir was stimulated
557 with a block design paradigm that consisted of four 20s-on and 60s-off periods with the order
558 of stimulation frequencies pseudorandomized (**Fig. 1B**). Typically, three fMRI sessions were
559 performed for each animal (i.e., five scans per session covering the five different frequencies).

560 **MRI acquisition procedure.** All MRI experiments were carried out on a 7T MRI scanner
561 (ParaVision v5.1, PharmaScan 70/16, Bruker Biospin GmbH, Ettlingen, Germany) using a
562 transmit-only birdcage coil in combination with an actively decoupled single-channel receive-
563 only surface coil. Scout T2-weighted (T2W) images were first obtained using a rapid
564 acquisition with relaxation enhancement (RARE) sequence for accurate positioning and as an
565 anatomical reference with field of view (FOV) = 32 × 32 mm$^2$, matrix = 256 × 256, RARE
566 factor = 8, echo time (TE) = 36 ms, and repetition time (TR) = 4200 ms. Seventeen contiguous
567 1 mm slices were then positioned in the transverse orientation according to the rat brain atlas
568 to cover most of the brain from the OB to the cerebellum. All fMRI measurements were made

569 using a single-shot gradient-echo echo-planar imaging (GE-EPI) sequence with FOV = 32 ×
570 32 $mm^2$, matrix = 64 × 64, flip angle = 56°, and TE/TR = 20/1000 ms.

571 **fMRI data analysis.** fMRI analysis was performed using the procedure established in our
572 previous studies[28-31,45,95]. For each fMRI session, all GE-EPI images were first corrected for
573 slice timing differences and then realigned to the mean image of the first fMRI scan using the
574 SPM12 fMRI toolbox (Wellcome Department of Imaging Neuroscience, University College
575 London, UK). fMRI scans suffering from motion artifacts (i.e., voxel shifts > 0.05 mm detected
576 by realignment) and sudden physiological changes (i.e., abrupt changes in respiration pattern,
577 heart rate, and oxygen saturation level) were discarded. After resampling EPI and T2 images
578 to 128 × 128 × 17, the EPI images from each animal were first registered to their respective
579 T2W images. T2W images from each animal were then co-registered to a custom-made brain
580 template acquired from separate age-matched rats with identical T2 scanning parameters using
581 affine transformation and Gaussian smoothing to maximize normalized mutual information
582 (SPM12). The transformation matrix was then applied to co-register the fMRI EPI volumes.
583 Voxel-wise linear detrending with least-squares estimation was subsequently performed
584 temporally for the EPI volumes to eliminate any baseline drift caused by physiological noise
585 and/or system instability. For individual animals, data from the three fMRI sessions were
586 smoothed (full width at half maximum, FWHM = 1 pixel with no out-of-plane smoothing), and
587 high pass filtered (128 s). Then, a general linear model (GLM) was applied to calculate the
588 response coefficient (β) maps for each stimulus. Student's t-test was performed to identify
589 activated voxels using the threshold $P < 0.001$ (t value > 3.1). BOLD signal profiles were then
590 extracted from regions of interest (ROIs) delineated from the rat brain atlas for further
591 evaluation. These steps performed at the individual animal level were done to ensure that visual
592 inspection and comparison of the data quality across animals could be conducted before group-
593 level analysis. At the group level, resliced, realigned and co-registered EPI images
594 corresponding to the same fMRI session and stimulation frequency were averaged across
595 animals. Similar smoothing, filtering, and GLM processes were then applied to generate group-
596 averaged BOLD activation maps with a threshold of $P < 0.001$. These thresholded activation
597 maps were further corrected for multiple comparisons (i.e., masked) with masks generated from
598 one-sample group level t-tests using nonparametric inference with threshold-free cluster
599 enhancement multiple comparison correction of family wise-error rate (TFCE-FWE, $P < 0.05$).
600 For the third fMRI session in experiments stimulating the AON and Pir, TFCE-FWE was not
601 applied in the masking of thresholded BOLD activation maps were only masked with the

602 group-level masks generated from one-sample group-level t-tests without TFCE-FWE
603 corrections (no activations after t-tests and TFCE-FWE corrections, $t > 3.1$).BOLD signal
604 profiles for each ROI were generated by averaging those extracted earlier from individual
605 animals.

606 In the fMRI experiments upon 1 Hz stimulations of OB, AON and Pir, quantification of the
607 strength of neural activity at downstream activation targets was performed separately for the
608 three consecutive fMRI sessions in each animal. First, the cumulative area under the BOLD
609 signal profile (AUC) for each atlas-defined ROI was computed. Here, only the area during the
610 four 20-s-on period of optogenetic stimulation was considered. Given that the BOLD response
611 onset in our experiments was ~3 s after the presentation of the stimulus, we systematically
612 delayed our area under BOLD signal profile measurements by 3 s. Second, the computed AUCs
613 were grouped into five networks such as the primary olfactory (OB, AON, Pir, tenia tecta, TT,
614 entorhinal cortex, Ent and olfactory tubercle, Tu), limbic (cingulate, Cg, orbitofrontal cortex,
615 OFC, insular, Ins and amygdala, Amg), striatal (nucleus accumbens, NAc and ventral caudate
616 putamen, vCPu), hippocampal (ventral hippocampus, vHP) and sensorimotor (motor, MC,
617 somatosensory, S1, auditory, AC and visual, V1, cortices). Third, BOLD activation strength
618 for each defined network was then measured. Here, the AUC of each network was normalized
619 to the AUC of all five networks. Lastly, the BOLD activation strengths for each network were
620 statistically compared between the three different fMRI stimulation experiments targeting OB
621 excitatory neurons, and OB afferents at AON and Pir, respectively (outlier detection with
622 nonlinear regression & false discovery rate at 1 %, Tukey's multiple comparisons test). Note
623 that direct comparisons between AUCs of each downstream target from the three separate
624 optogenetic fMRI experiments were not considered as they are likely erroneous given the
625 differences in absolute BOLD signal amplitudes. For example, BOLD signal amplitudes in Pir
626 stimulation experiments were generally weaker than OB and AON stimulations. The variations
627 here are likely caused by differences in ChR2 transfection volumes in OB excitatory neurons
628 and OB afferents at AON/Pir, including the population size of neurons/axonal terminals
629 stimulated. Note that the vast majority of OB neurons are interneurons, and not projection
630 neurons to OB and AON[37].

631 Comparison of BOLD power between fMRI sessions (i.e., 1$^{st}$ vs. 2$^{nd}$, 1$^{st}$ vs. 3$^{rd}$ fMRI session)
632 upon 1 Hz stimulation was done using Dunnett's multiple comparisons test to evaluate
633 olfactory adaptation under repetitive OB/AON/Pir stimulation. Normalized BOLD power was
634 only shown for display (not all data points were shown, because some values were extremely

635 huge) with statistical results calculated based on true BOLD power comparison (**Fig. S5**).
636 When comparing the BOLD power between healthy vs. aged rats upon first 1 Hz OB
637 stimulation, we conducted an uncorrected Fisher's LSD test (**Fig. 7B**).

638 **Spectral dynamic causal modeling (sDCM), and statistical analyses.** To parametrize the
639 downstream effects of OB-, AON- and Pir-driven neural activities on selected targets in the
640 right brain hemisphere (i.e., same hemispheric side to the optogenetically-stimulated region)
641 in healthy and aged animals, we further analyzed the BOLD fMRI data upon 1 Hz stimulation
642 using sDCM[26]. A six-node brain network model was defined, encompassing connections
643 between regions in the primary olfactory (OB, AON and Pir), striatal (vCPu) and limbic (Amg)
644 networks (**Fig. 4A**). Specifically, sDCM was utilized to computationally model the effective
645 connectivity strength of these downstream connections in OB, AON and Pir stimulation of
646 healthy animals, and OB stimulation data of aged animals. To avoid over-fitting of the data,
647 the BOLD signals were band-pass filtered with low cutoff frequency at 1/128 Hz and a range
648 of high cutoff frequencies at 0.1-0.3 Hz. We then evaluated the connectivity parameters from
649 the choice of 21 high cutoff frequencies with a step size of 0.01 Hz. We selected the optimal
650 high cutoff frequency for each stimulation target (i.e., OB, AON, Pir) that maximized the
651 weighted sum of scores for all modeled connections (significant, $P < 0.05$, score = 1; close to
652 significant, $0.05 < P < 0.1$, score = 0.5; FDR corrected). The optimal high cutoff frequencies
653 were 0.1, 0.18 and 0.14 Hz for OB, AON and Pir stimulations, respectively, in healthy animals,
654 and 0.1 Hz for OB stimulation in aged animals. Stochastic sDCM has been demonstrated to
655 perform better compared to deterministic modeling[26]. Here, we utilized Bayesian model
656 selection to determine the autoregressive model order (e.g., autoregressive models of order one,
657 AR1; order two, AR2), which was used to parameterize neural fluctuations and observed noise
658 in stochastic models. We then applied Bayesian model averaging (BMA) to generate the mean
659 effective connectivity for each defined connection since we did not obtain a clear winning
660 autoregressive model order. Following BMA, the mean effective connectivity was statistically
661 compared across animals and summarized in the form of connectivity matrices (**Fig. 4B**, n =
662 11, n = 11 and n = 9 for OB, AON and Pir stimulation in healthy animals; n = 13 for OB
663 stimulation in aged animals; one-sample t-test with FDR correction). We further quantified the
664 differences in the effective connectivity of AON-related vs. Pir-related connections to
665 downstream targets such as Ent, vCPu and Amg by conducting paired t-test with FDR
666 correction (**Fig. 4C**). Unpaired t-test was used to compare the effective connectivity of AON-
667 related and Pir-related connections between healthy and aged animals (**Fig. 7D**).

668 **Multi-site local field potential (LFP) recordings and analyses.** Electrophysiological
669 recordings were performed under the same anesthesia protocols and similar physiological
670 conditions as in the fMRI experiments with body temperature maintained using a heating pad.
671 Guided by the fMRI findings, craniotomies were conducted and dura matter was removed with
672 reference to the ROIs of ipsilateral OB (+7.5 mm anterior to Bregma, +1.8 mm ML), AON
673 (+5.2 mm anterior to Bregma, +1.8 mm ML), Pir (+4.2 mm anterior to Bregma, +3.1 mm ML),
674 vCPu (+2 mm anterior to Bregma, +2.7 mm ML), Amg (-3 mm posterior to Bregma, +3.8 mm
675 ML)/ V1 (-6 mm posterior to Bregma, +4.2 mm ML), vHP (-6.4 mm posterior to Bregma, +6.4
676 mm ML) / dHP (-3.6 mm posterior to Bregma, +2.4 mm ML). For coverage of the majority of
677 layers in the dentate gyrus of ipsilateral vHP/dHP, a linear microelectrode silicon array (16
678 recording channels equally spaced at 100 μm; 1.5 MΩ impedance; NeuroNexus Technologies,
679 Ann Arbor, MI) was inserted perpendicularly to the brain surface with the tip of the linear array
680 approximately 4.5 mm/3.7 mm below the dura matter via micromanipulators (Narishige,
681 Amityville, NY). For other regions, single tungsten microelectrodes with 2.0 MΩ and 10 μm
682 tip diameter were utilized (OB: -1.8 mm DV; AON: -4.3 mm DV; Pir: -5.4 mm DV; vCPu: -
683 5.4 mm DV; V1: -1.1 mm DV; Amg: -8.4 mm DV). Fiber and a single channel electrode were
684 constructed into an optrode[97] and were implanted following identical procedures as described
685 for optogenetic fMRI experiments. LFP data were acquired using a multi-channel
686 neurophysiology recording system (sampling frequency: 24 kHz; notch-filter: 50 Hz, 100 Hz,
687 and 150 Hz; Tucker Davis Technologies/TDT, Alachua, FL). Synchronized laser stimulation
688 was controlled by the same system, and the trigger signal for blue light pulse trains was
689 recorded simultaneously with the extracellular recording data. Experimental paradigms were
690 identical to those used in fMRI experiments.

691 After recordings, raw data were bandpass-filtered (0.01-150 Hz) and down-sampled to 1 kHz
692 using MATLAB. Individual LFP and group-averaged LFP traces were generated. Averaged
693 LFP traces were presented with standard error mean to reflect the reproducibility across
694 animals as shown by our previous analyses and literature[28,29,45,98-100]. The latency of evoked
695 LFPs was measured from the onset of light pulse to the first appreciable peak location (i.e.,
696 either negative or positive). To quantify the optogenetically evoked neural activity power
697 during the 20-s optogenetic stimulation block, the area under absolute LFP traces was measured
698 as LFP power during the optogenetic stimulation. Given that the LFP response onset was a few
699 milliseconds after the presentation of the stimulus, no time delay for area under the LFP power
700 measurements (**Fig. 6**).

701 **Histology, immunohistochemistry, and confocal imaging.** To confirm the specific
702 expression of ChR2-mCherry in the OB excitatory neurons and the axonal inputs to AON/Pir,
703 histology was performed according to the previously published procedure[28-31,45,95]. Upon
704 completion of experiments, a selected number of optogenetically transfected animals (n = 3 for
705 OB; n = 2 for AON/Pir) were anesthetized with pentobarbital and then transcardially perfused
706 with ice-cold 4% paraformaldehyde (PFA) in phosphate-buffered saline (PBS). The brains
707 were equilibrated in 20% sucrose in PBS at 4 °C overnight. Axial sections (40 μm) were
708 prepared on a freezing microtome (model 860, AO Scientific Instruments). Consecutive
709 sections were mounted and examined with a laser confocal microscope (Carl Zeiss
710 LSM780/LSM980). For immunohistochemistry, free-floating sections were processed with 5%
711 normal goat serum and 0.3% Triton X-100 in PBS with primary antibodies against rabbit
712 polyclonal to CaMKIIα (1:400; Abcam) at 4 °C for 24 h. After washing with PBS, sections
713 were then incubated for 2 h at room temperature with secondary antibodies Alexa Fluor 647
714 conjugate goat anti-rabbit IgG and Alexa Fluor 488 conjugate goat anti-guinea pig IgG (both
715 1:500; Molecular Probe). Slices were then washed and mounted using FluoroShield mounting
716 medium with DAPI (Abcam). Double or triple immunofluorescence was assessed with a laser
717 confocal microscope (Carl Zeiss LSM780/LSM980).

## Acknowledgement

This work was supported by the Hong Kong Research Grant Council (HKU17127723, HKU17127021 and HKU17104020 to A.T.L. Leong, and HKU17127523, HKU17127022, HKU17127121 and HKU17112120 to E.X. Wu) and Lam Woo Foundation to E.X. Wu. We would like to thank Drs. L.W. Lim, P.S. Chong, E. Wong, and Ms. S. Kwok for their advice and/or technical assistance. We would also like to thank Dr. K. Deisseroth who provided us with the ChR2 viral construct.

## Author Contributions

Study design and conceptualization: T.M., X.W., A.T.L.L. and E.X.W.. Animal fMRI experiments: T.M.. Animal fMRI data analysis: T.M., X.W., A.T.L.L. and X.L.. Electrophysiology experiments: T.M. and J.W.. Electrophysiology data analysis: T.M., X.W. and A.T.L.L.. Visualization: T.M., A.T.L.L., X.W., X.L. and L.X.. Suggestions: X.W., A.T.L.L. and L.X.. Supervision: A.T.L.L., E.X.W., X.W. and P.C.. Original draft writing: T.M. and A.T.L.L.. Writing-review and editing: A.T.L.L., E.X.W., T.M. and X.W..

## Competing Interests

The authors declare no competing interests.

## Additional Information

Supplementary information accompanies this paper.

## References


1. Ache, B.W. & Young, J.M. Olfaction: diverse species, conserved principles. *Neuron* **48**, 417-430 (2005).
2. Leinwand, S.G. & Chalasani, S.H. Olfactory networks: from sensation to perception. *Curr Opin Genet Dev* **21**, 806-811 (2011).
3. Buck, L. & Axel, R. A novel multigene family may encode odorant receptors: a molecular basis for odor recognition. *Cell* **65**, 175-187 (1991).
4. Laurent, G. Olfactory network dynamics and the coding of multidimensional signals. *Nat Rev Neurosci* **3**, 884-895 (2002).
5. Mori, K. & Sakano, H. Olfactory Circuitry and Behavioral Decisions. *Annu Rev Physiol* **83**, 231-256 (2021).
6. Miyamichi, K., Amat, F., Moussavi, F., Wang, C., Wickersham, I., Wall, N.R., Taniguchi, H., Tasic, B., Huang, Z.J., He, Z., Callaway, E.M., Horowitz, M.A. & Luo, L. Cortical representations of olfactory input by trans-synaptic tracing. *Nature* **472**, 191-196 (2011).
7. Schaffer, E.S., Stettler, D.D., Kato, D., Choi, G.B., Axel, R. & Abbott, L.F. Odor Perception on the Two Sides of the Brain: Consistency Despite Randomness. *Neuron* **98**, 736-742 e733 (2018).
8. Chong, E., Moroni, M., Wilson, C., Shoham, S., Panzeri, S. & Rinberg, D. Manipulating synthetic optogenetic odors reveals the coding logic of olfactory perception. *Science (New York, N.Y.)* **368**(2020).
9. Lynn, C.W. & Bassett, D.S. The physics of brain network structure, function and control. *Nature Reviews Physics* **1**, 318-332 (2019).
10. Suarez, L.E., Markello, R.D., Betzel, R.F. & Misic, B. Linking Structure and Function in Macroscale Brain Networks. *Trends Cogn Sci* **24**, 302-315 (2020).
11. Seguin, C., Sporns, O. & Zalesky, A. Brain network communication: concepts, models and applications. *Nat Rev Neurosci* **24**, 557-574 (2023).
12. Lee, J.H., Liu, Q. & Dadgar-Kiani, E. Solving brain circuit function and dysfunction with computational modeling and optogenetic fMRI. *Science (New York, N.Y.)* **378**, 493-499 (2022).
13. Mobley, A.S., Rodriguez-Gil, D.J., Imamura, F. & Greer, C.A. Aging in the olfactory system. *Trends Neurosci* **37**, 77-84 (2014).
14. Doty, R.L. Olfactory dysfunction in neurodegenerative diseases: is there a common pathological substrate? *The Lancet Neurology* **16**, 478-488 (2017).
15. Xydakis, M.S., Albers, M.W., Holbrook, E.H., Lyon, D.M., Shih, R.Y., Frasnelli, J.A., Pagenstecher, A., Kupke, A., Enquist, L.W. & Perlman, S. Post-viral effects of COVID-19 in the olfactory system and their implications. *The Lancet Neurology* **20**, 753-761 (2021).
16. Dolgin, E. The science behind COVID's assault on smell. *Nature* **606**, S5-S6 (2022).
17. Lempriere, S. Olfactory network function altered in COVID-19. *Nat Rev Neurol* **19**, 326 (2023).
18. Kurahashi, T. & Menini, A. Mechanism of odorant adaptation in the olfactory receptor cell. *Nature* **385**, 725-729 (1997).
19. Kadohisa, M. & Wilson, D.A. Olfactory cortical adaptation facilitates detection of odors against background. *J Neurophysiol* **95**, 1888-1896 (2006).
20. Xu, F., Kida, I., Hyder, F. & Shulman, R.G. Assessment and discrimination of odor stimuli in rat olfactory bulb by dynamic functional MRI. *Proc Natl Acad Sci U S A* **97**, 10601-10606 (2000).

21. Zhao, F., Meng, X., Lu, S., Hyde, L.A., Kennedy, M.E., Houghton, A.K., Evelhoch, J.L. & Hines, C.D.G. fMRI study of olfactory processing in mice under three anesthesia protocols: Insight into the effect of ketamine on olfactory processing. *Neuroimage* **213**, 116725 (2020).
22. Zhou, G., Lane, G., Cooper, S.L., Kahnt, T. & Zelano, C. Characterizing functional pathways of the human olfactory system. *Elife* **8**, e47177 (2019).
23. Weiss, T., Soroka, T., Gorodisky, L., Shushan, S., Snitz, K., Weissgross, R., Furman-Haran, E., Dhollander, T. & Sobel, N. Human Olfaction without Apparent Olfactory Bulbs. *Neuron* **105**, 35-45 e35 (2020).
24. Manzini, I., Schild, D. & Di Natale, C. Principles of odor coding in vertebrates and artificial chemosensory systems. *Physiol Rev* **102**, 61-154 (2022).
25. Brunert, D., Medinaceli Quintela, R. & Rothermel, M. The anterior olfactory nucleus revisited - An emerging role for neuropathological conditions? *Prog Neurobiol* **228**, 102486 (2023).
26. Bernal-Casas, D., Lee, H.J., Weitz, A.J. & Lee, J.H. Studying Brain Circuit Function with Dynamic Causal Modeling for Optogenetic fMRI. *Neuron* **93**, 522-532 e525 (2017).
27. Boyden, E.S., Zhang, F., Bamberg, E., Nagel, G. & Deisseroth, K. Millisecond-timescale, genetically targeted optical control of neural activity. *Nat Neurosci* **8**, 1263-1268 (2005).
28. Leong, A.T.L., Chan, R.W., Gao, P.P., Chan, Y.S., Tsia, K.K., Yung, W.H. & Wu, E.X. Long-range projections coordinate distributed brain-wide neural activity with a specific spatiotemporal profile. *Proc Natl Acad Sci U S A* **113**, E8306-E8315 (2016).
29. Chan, R.W., Leong, A.T.L., Ho, L.C., Gao, P.P., Wong, E.C., Dong, C.M., Wang, X., He, J., Chan, Y.S., Lim, L.W. & Wu, E.X. Low-frequency hippocampal-cortical activity drives brain-wide resting-state functional MRI connectivity. *Proc Natl Acad Sci U S A* **114**, E6972-E6981 (2017).
30. Leong, A.T.L., Gu, Y., Chan, Y.S., Zheng, H., Dong, C.M., Chan, R.W., Wang, X., Liu, Y., Tan, L.H. & Wu, E.X. Optogenetic fMRI interrogation of brain-wide central vestibular pathways. *Proc Natl Acad Sci U S A* **116**, 10122-10129 (2019).
31. Wang, X., Leong, A.T.L., Tan, S.Z.K., Wong, E.C., Liu, Y., Lim, L.W. & Wu, E.X. Functional MRI reveals brain-wide actions of thalamically-initiated oscillatory activities on associative memory consolidation. *Nat Commun* **14**, 2195 (2023).
32. Aqrabawi, A.J. & Kim, J.C. Olfactory memory representations are stored in the anterior olfactory nucleus. *Nat Commun* **11**, 1246 (2020).
33. Poo, C., Agarwal, G., Bonacchi, N. & Mainen, Z.F. Spatial maps in piriform cortex during olfactory navigation. *Nature* **601**, 595-599 (2022).
34. Strauch, C. & Manahan-Vaughan, D. Orchestration of Hippocampal Information Encoding by the Piriform Cortex. *Cereb Cortex* **30**, 135-147 (2020).
35. Aqrabawi, A.J. & Kim, J.C. Hippocampal projections to the anterior olfactory nucleus differentially convey spatiotemporal information during episodic odour memory. *Nat Commun* **9**, 2735 (2018).
36. Moberly, A.H., Schreck, M., Bhattarai, J.P., Zweifel, L.S., Luo, W. & Ma, M. Olfactory inputs modulate respiration-related rhythmic activity in the prefrontal cortex and freezing behavior. *Nat Commun* **9**, 1528 (2018).
37. Ennis, M., Puche, A.C., Holy, T. & Shipley, M.T. The Olfactory System. in *The Rat Nervous System* 761-803 (2015).
38. Bekkers, J.M. & Suzuki, N. Neurons and circuits for odor processing in the piriform cortex. *Trends Neurosci* **36**, 429-438 (2013).
39. Brunjes, P.C., Illig, K.R. & Meyer, E.A. A field guide to the anterior olfactory nucleus (cortex). *Brain Res Brain Res Rev* **50**, 305-335 (2005).

40. Seghier, M.L. & Friston, K.J. Network discovery with large DCMs. *Neuroimage* **68**, 181-191 (2013).
41. Russo, M.J., Franks, K.M., Oghaz, R., Axel, R. & Siegelbaum, S.A. Synaptic organization of anterior olfactory nucleus inputs to piriform cortex. *J Neurosci* (2020).
42. Chae, H., Banerjee, A., Dussauze, M. & Albeanu, D.F. Long-range functional loops in the mouse olfactory system and their roles in computing odor identity. *Neuron* **110**, 3970-+ (2022).
43. Sato, T.K., Hausser, M. & Carandini, M. Distal connectivity causes summation and division across mouse visual cortex. *Nat Neurosci* **17**, 30-32 (2014).
44. Ciocchi, S., Passecker, J., Malagon-Vina, H., Mikus, N. & Klausberger, T. Brain computation. Selective information routing by ventral hippocampal CA1 projection neurons. *Science (New York, N.Y.)* **348**, 560-563 (2015).
45. Leong, A.T.L., Wang, X., Wong, E.C., Dong, C.M. & Wu, E.X. Neural activity temporal pattern dictates long-range propagation targets. *Neuroimage* **235**, 118032 (2021).
46. Schoppa, N.E. Synchronization of olfactory bulb mitral cells by precisely timed inhibitory inputs. *Neuron* **49**, 271-283 (2006).
47. Davison, I.G. & Ehlers, M.D. Neural circuit mechanisms for pattern detection and feature combination in olfactory cortex. *Neuron* **70**, 82-94 (2011).
48. Tsuji, T., Tsuji, C., Lozic, M., Ludwig, M. & Leng, G. Coding of odors in the anterior olfactory nucleus. *Physiol Rep* **7**, e14284 (2019).
49. McCollum, J., Larson, J., Otto, T., Schottler, F., Granger, R. & Lynch, G. Short-latency single unit processing in olfactory cortex. *J Cogn Neurosci* **3**, 293-299 (1991).
50. McGinley, M.J. & Westbrook, G.L. Membrane and synaptic properties of pyramidal neurons in the anterior olfactory nucleus. *Journal of Neurophysiology* **105**, 1444-1453 (2011).
51. Bitzenhofer, S.H., Westeinde, E.A., Zhang, H.B. & Isaacson, J.S. Rapid odor processing by layer 2 subcircuits in lateral entorhinal cortex. *Elife* **11**(2022).
52. Albrecht, J. & Wiesmann, M. Olfactory Pathways. in *Encyclopedia of Neuroscience* (eds. Binder, M.D., Hirokawa, N. & Windhorst, U.) 3003-3006 (Springer Berlin Heidelberg, Berlin, Heidelberg, 2009).
53. Gadziola, M.A., Tylicki, K.A., Christian, D.L. & Wesson, D.W. The olfactory tubercle encodes odor valence in behaving mice. *J Neurosci* **35**, 4515-4527 (2015).
54. Gire, D.H., Restrepo, D., Sejnowski, T.J., Greer, C., De Carlos, J.A. & Lopez-Mascaraque, L. Temporal Processing in the Olfactory System: Can We See a Smell? *Neuron* **78**, 416-432 (2013).
55. Andrews, E.F., Pascalau, R., Horowitz, A., Lawrence, G.M. & Johnson, P.J. Extensive Connections of the Canine Olfactory Pathway Revealed by Tractography and Dissection. *J Neurosci* **42**, 6392-6407 (2022).
56. Li, Y.D., Xu, J.M., Liu, Y.F., Zhu, J., Liu, N., Zeng, W.B., Huang, N., Rasch, M.J., Jiang, H.F., Gu, X., Li, X., Luo, M.H., Li, C.Y., Teng, J.L., Chen, J.G., Zeng, S.Q., Lin, L.N. & Zhang, X.H. A distinct entorhinal cortex to hippocampal CA1 direct circuit for olfactory associative learning. *Nature Neuroscience* **20**, 559-+ (2017).
57. Markopoulos, F., Rokni, D., Gire, D.H. & Murthy, V.N. Functional Properties of Cortical Feedback Projections to the Olfactory Bulb. *Neuron* **76**, 1175-1188 (2012).
58. Debanne, D., Campanac, E., Bialowas, A., Carlier, E. & Alcaraz, G. Axon physiology. *Physiol Rev* **91**, 555-602 (2011).
59. Sadigh-Eteghad, S., Majdi, A., McCann, S.K., Mahmoudi, J., Vafaee, M.S. & Macleod, M.R. D-galactose-induced brain ageing model: A systematic review and meta-analysis on cognitive outcomes and oxidative stress indices. *PloS one* **12**, e0184122 (2017).

60. Shwe, T., Pratchayasakul, W., Chattipakorn, N. & Chattipakorn, S.C. Role of D-galactose-induced brain aging and its potential used for therapeutic interventions. *Exp Gerontol* **101**, 13-36 (2018).
61. Brann, D.H. & Datta, S.R. Finding the Brain in the Nose. *Annual Review of Neuroscience, Vol 43* **43**, 277-295 (2020).
62. Lane, G., Zhou, G., Noto, T. & Zelano, C. Assessment of direct knowledge of the human olfactory system. *Exp Neurol* **329**, 113304 (2020).
63. Reinert, J.K. & Fukunaga, I. The facets of olfactory learning. *Curr Opin Neurobiol* **76**, 102623 (2022).
64. Bothwell, A.R., Resnick, S.M., Ferrucci, L. & Tian, Q. Associations of olfactory function with brain structural and functional outcomes. A systematic review. *Ageing Res Rev* **92**, 102095 (2023).
65. Pellegrino, R., Sinding, C., de Wijk, R.A. & Hummel, T. Habituation and adaptation to odors in humans. *Physiol Behav* **177**, 13-19 (2017).
66. Sinding, C., Valadier, F., Al-Hassani, V., Feron, G., Tromelin, A., Kontaris, I. & Hummel, T. New determinants of olfactory habituation. *Sci Rep* **7**, 41047 (2017).
67. Zufall, F. & Leinders-Zufall, T. The cellular and molecular basis of odor adaptation. *Chem Senses* **25**, 473-481 (2000).
68. Ogg, M.C., Bendahamane, M. & Fletcher, M.L. Habituation of glomerular responses in the olfactory bulb following prolonged odor stimulation reflects reduced peripheral input. *Frontiers in Molecular Neuroscience* **8**(2015).
69. Storace, D.A. & Cohen, L.B. The Mammalian Olfactory Bulb Contributes to the Adaptation of Odor Responses: A Second Perceptual Computation Carried Out by the Bulb. *eNeuro* **8**(2021).
70. Wilson, D.A. Habituation of odor responses in the rat anterior piriform cortex. *J Neurophysiol* **79**, 1425-1440 (1998).
71. Kadohisa, M. & Wilson, D.A. Olfactory cortical adaptation facilitates detection of odors against background. *Journal of Neurophysiology* **95**, 1888-1896 (2006).
72. Xia, C.Z., Adjei, S. & Wesson, D.W. Coding of odor stimulus features among secondary olfactory structures. *J Neurophysiol* **114**, 736-745 (2015).
73. Chaudhury, D., Manella, L., Arellanos, A., Escanilla, O., Cleland, T.A. & Linster, C. Olfactory Bulb Habituation to Odor Stimuli. *Behav Neurosci* **124**, 490-499 (2010).
74. Haberly, L.B. & Price, J.L. Association and commissural fiber systems of the olfactory cortex of the rat. *J Comp Neurol* **178**, 711-740 (1978).
75. Illig, K.R. & Eudy, J.D. Contralateral Projections of the Rat Anterior Olfactory Nucleus. *Journal of Comparative Neurology* **512**, 115-123 (2009).
76. Grobman, M., Dalal, T., Lavian, H., Shmuel, R., Belelovsky, K., Xu, F., Korngreen, A. & Haddad, R. A Mirror-Symmetric Excitatory Link Coordinates Odor Maps across Olfactory Bulbs and Enables Odor Perceptual Unity. *Neuron* **99**, 800-813 e806 (2018).
77. Aqrabawi, A.J., Browne, C.J., Dargaei, Z., Garand, D., Khademullah, C.S., Woodin, M.A. & Kim, J.C. Top-down modulation of olfactory-guided behaviours by the anterior olfactory nucleus pars medialis and ventral hippocampus. *Nat Commun* **7**, 13721 (2016).
78. Medinaceli Quintela, R., Bauer, J., Wallhorn, L., Le, K., Brunert, D. & Rothermel, M. Dynamic Impairment of Olfactory Behavior and Signaling Mediated by an Olfactory Corticofugal System. *J Neurosci* **40**, 7269-7285 (2020).
79. Aqrabawi, A.J. & Kim, J.C. Topographic Organization of Hippocampal Inputs to the Anterior Olfactory Nucleus. *Front Neuroanat* **12**, 12 (2018).
80. Levinson, M., Kolenda, J.P., Alexandrou, G.J., Escanilla, O., Cleland, T.A., Smith, D.M. & Linster, C. Context-dependent odor learning requires the anterior olfactory nucleus. *Behav Neurosci* **134**, 332-343 (2020).

81. Luskin, M.B. & Price, J.L. The topographic organization of associational fibers of the olfactory system in the rat, including centrifugal fibers to the olfactory bulb. *J Comp Neurol* **216**, 264-291 (1983).
82. Chen, Z. & Padmanabhan, K. Top-down feedback enables flexible coding strategies in the olfactory cortex. *Cell Rep* **38**, 110545 (2022).
83. Russo, M.J., Franks, K.M., Oghaz, R., Axel, R. & Siegelbaum, S.A. Synaptic Organization of Anterior Olfactory Nucleus Inputs to Piriform Cortex. *J Neurosci* **40**, 9414-9425 (2020).
84. Mori, K. & Sakano, H. Olfactory Circuitry and Behavioral Decisions. *Annual Review of Physiology, Vol 83* **83**, 231-256 (2021).
85. Bolding, K.A. & Franks, K.M. Recurrent cortical circuits implement concentration-invariant odor coding. *Science (New York, N.Y.)* **361**(2018).
86. Stettler, D.D. & Axel, R. Representations of odor in the piriform cortex. *Neuron* **63**, 854-864 (2009).
87. Datiche, F. & Cattarelli, M. Reciprocal and topographic connections between the piriform and prefrontal cortices in the rat: A tracing study using the B subunit of the cholera toxin. *Brain Research Bulletin* **41**, 391-398 (1996).
88. Johnson, D.M.G., Illig, K.R., Behan, M. & Haberly, L.B. New features of connectivity in piriform cortex visualized by intracellular injection of pyramidal cells suggest that "primary" olfactory cortex functions like "association" cortex in other sensory systems. *J Neurosci* **20**, 6974-6982 (2000).
89. Garrison, J.L. & Knight, Z.A. Linking smell to metabolism and aging. *Science (New York, N.Y.)* **358**, 718-719 (2017).
90. Shen, Y.X., Xu, S.Y., Wei, W., Sun, X.X., Yang, J., Liu, L.H. & Dong, C. Melatonin reduces memory changes and neural oxidative damage in mice treated with D-galactose. *J Pineal Res* **32**, 173-178 (2002).
91. Tian, J., Ishibashi, K., Ishibashi, K., Reiser, K., Grebe, R., Biswal, S., Gehlbach, P. & Handa, J.T. Advanced glycation endproduct-induced aging of the retinal pigment epithelium and choroid: A comprenensive transcriptionai response. *Proceedings of the National Academy of Sciences of the United States of America* **102**, 11846-11851 (2005).
92. Esiri, M.M. & Wilcock, G.K. The olfactory bulbs in Alzheimer's disease. *J Neurol Neurosurg Psychiatry* **47**, 56-60 (1984).
93. Foveau, B., Albrecht, S., Bennett, D.A., Correa, J.A. & LeBlanc, A.C. Increased Caspase-6 activity in the human anterior olfactory nuclei of the olfactory bulb is associated with cognitive impairment. *Acta Neuropathol Com* **4**(2016).
94. Ubeda-Bañon, I., Saiz-Sanchez, D., Flores-Cuadrado, A., Rioja-Corroto, E., Gonzalez-Rodriguez, M., Villar-Conde, S., Astillero-Lopez, V., Cabello-de la Rosa, J.P., Gallardo-Alcañiz, M.J., Vaamonde-Gamo, J., Relea-Calatayud, F., Gonzalez-Lopez, L., Mohedano-Moriano, A., Rabano, A. & Martinez-Marcos, A. The human olfactory system in two proteinopathies: Alzheimer's and Parkinson's diseases. *Transl Neurodegener* **9**(2020).
95. Leong, A.T.L., Wong, E.C., Wang, X. & Wu, E.X. Hippocampus Modulates Vocalizations Responses at Early Auditory Centers. *Neuroimage* **270**, 119943 (2023).
96. Yizhar, O., Fenno, L.E., Davidson, T.J., Mogri, M. & Deisseroth, K. Optogenetics in neural systems. *Neuron* **71**, 9-34 (2011).
97. Sparta, D.R., Stamatakis, A.M., Phillips, J.L., Hovelso, N., van Zessen, R. & Stuber, G.D. Construction of implantable optical fibers for long-term optogenetic manipulation of neural circuits. *Nat Protoc* **7**, 12-23 (2011).

98. Einevoll, G.T., Kayser, C., Logothetis, N.K. & Panzeri, S. Modelling and analysis of local field potentials for studying the function of cortical circuits. *Nat Rev Neurosci* **14**, 770-785 (2013).
99. Sakata, S. & Harris, K.D. Laminar structure of spontaneous and sensory-evoked population activity in auditory cortex. *Neuron* **64**, 404-418 (2009).
100. Quairiaux, C., Megevand, P., Kiss, J.Z. & Michel, C.M. Functional development of large-scale sensorimotor cortical networks in the brain. *J Neurosci* **31**, 9574-9584 (2011).

991 **Figure Legends**

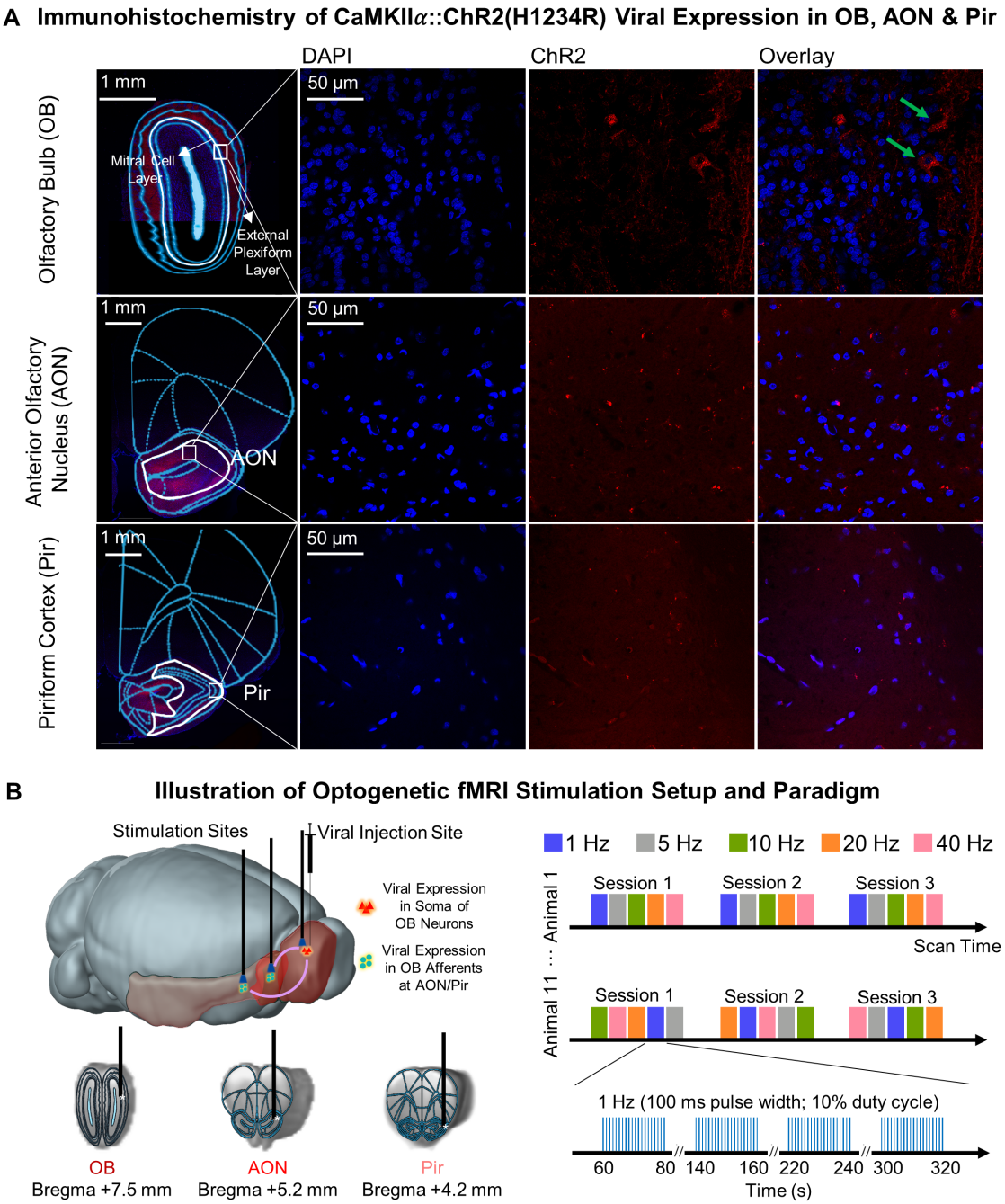


992
993 **Figure 1. Histological characterization of ChR2::CaMKIIα viral expression in the**
994 **olfactory bulb (OB) excitatory neurons and OB afferents at the anterior olfactory nucleus**
995 **(AON) and the piriform cortex (Pir), and optogenetic fMRI stimulation setup. (A)**
996 Confocal images, 10x magnification (Left) and 40x magnification (Right), of ChR2-mCherry
997 expression in histological slices covering OB, AON and Pir. Overlay of images co-stained for
998 the nuclear marker DAPI and mCherry in OB (Top) revealed ChR2 expression in the soma of
999 the mitral cell layer & external plexiform layer in OB (indicated by green arrows). Meanwhile,

1000 ChR2 expressions were found in OB afferents at AON and Pir (Middle & Bottom), indicated
1001 by no colocalization between mCherry and DAPI. **(B)** Illustration of three optogenetic
1002 stimulation targets, namely the OB excitatory neurons, and OB afferents in AON and Pir (Left),
1003 which were conducted in separate animal groups. T2-weighted anatomical MRI image showing
1004 the location of the implanted optical fiber (asterisk: stimulation target). Optogenetic fMRI
1005 block-designed stimulation paradigm (Right). Five different frequencies (1, 5, 10, 20, and 40
1006 Hz) were presented in a pseudorandomized order within each session. We repeated the
1007 stimulations for a total of three sessions in each animal fMRI experiment. All frequencies were
1008 presented at a 30% duty cycle except for 1 Hz, which was presented at a 10% duty cycle.

1009

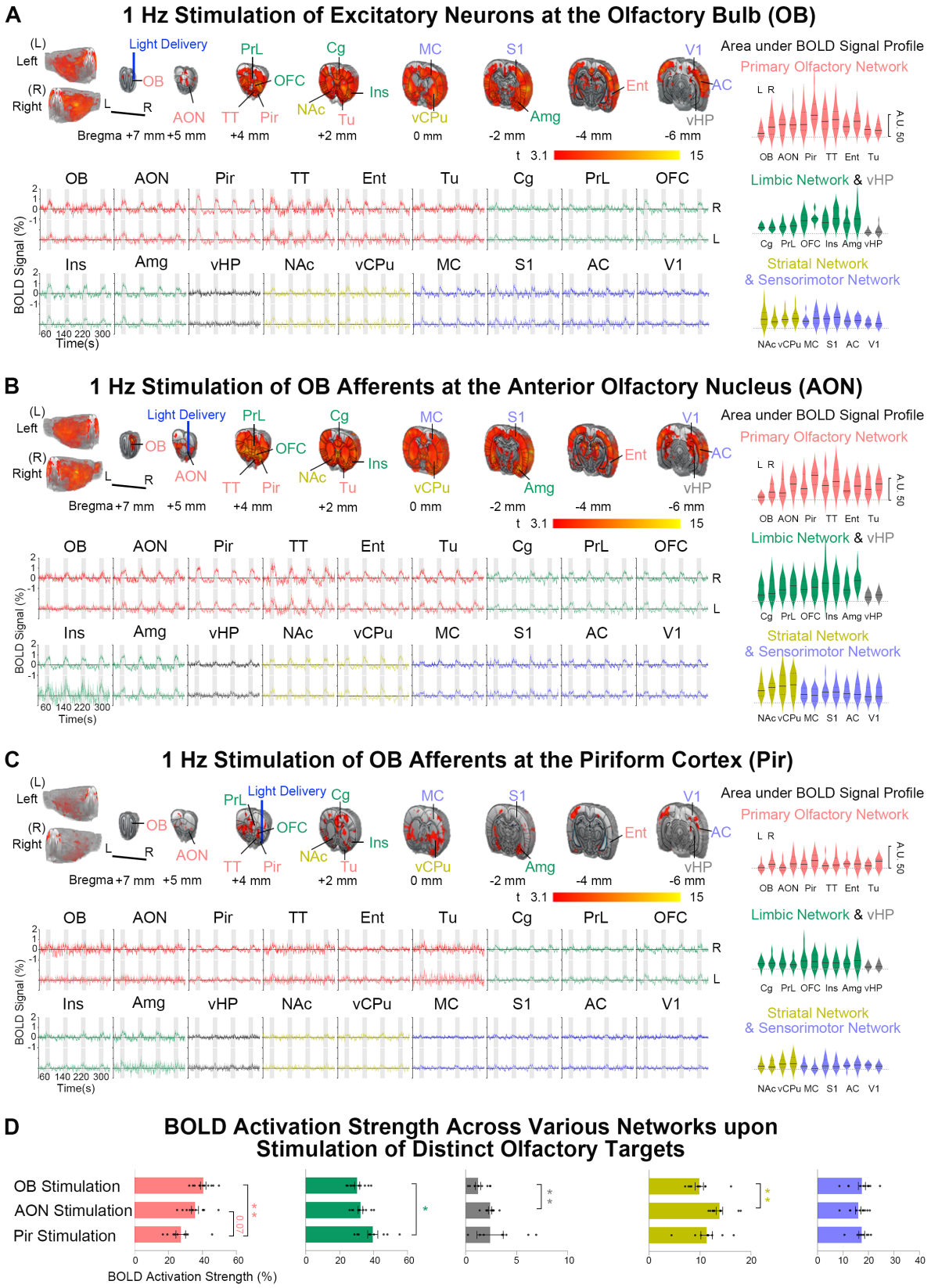


1010

1011 **Figure 2. Optogenetic excitation of OB excitatory neurons and OB afferents at AON and**

1012 **Pir recruit distinct brain-wide long-range olfactory networks.** Averaged BOLD activation

1013 maps and signal profiles (Left) upon 1 Hz stimulation of (**A**) OB excitatory neurons, (**B**) OB
1014 afferents in AON, and (**C**) OB afferents in Pir during the first fMRI session (n = 11 for fMRI
1015 experiments in A & B; n = 9 for C; t > 3.1 corresponding to $P < 0.001$; error bars indicate ±
1016 SEM), and the corresponding area under the BOLD signal profiles (AUC) for each atlas-
1017 defined region-of-interests (ROIs; Right). Note that the BOLD activation maps displayed in A-
1018 C were further corrected for multiple comparisons with threshold-free cluster enhancement
1019 with family-wise error rate (TFCE-FWE) at $P < 0.05$. (**D**) Summary of BOLD activation
1020 strength to quantify the extent of various brain networks engaged upon respective optogenetic
1021 stimulation of the three different primary olfactory stimulation targets. BOLD activation
1022 strength was computed as the ratio of AUC for each ROI over AUC of all ROIs (individual
1023 animal data points are shown; error bars indicate ± SEM; Tukey's multiple comparisons test;
1024 $^{**}P < 0.01$, and $^{*}P < 0.05$). OB-driven neural activities mainly activated the primary olfactory
1025 network (AON, Pir, TT, Ent and Tu). AON-driven neural activities were found to preferentially
1026 recruit the striatal (NAc and vCPu) and hippocampal networks (vHP), while Pir-driven
1027 activities strongly targeted the limbic network (Cg, PrL, OFC, Ins and Amg).
1028 *Abbreviations. Regions in primary olfactory network: olfactory bulb (OB), anterior olfactory*
1029 *nucleus (AON), piriform cortex (Pir), tenia tecta (TT), entorhinal cortex (Ent), olfactory*
1030 *tubercle (Tu); limbic network: cingulate (Cg), prelimbic cortex (PrL), orbitofrontal cortex*
1031 *(OFC), insular (Ins), amygdala (Amg); hippocampal network: ventral hippocampus (vHP);*
1032 *striatal network: nucleus accumbens (NAc), ventral caudate putamen (vCPu); sensorimotor*
1033 *network: motor (MC), somatosensory (S1), auditory (AC), visual (V1) cortex.*

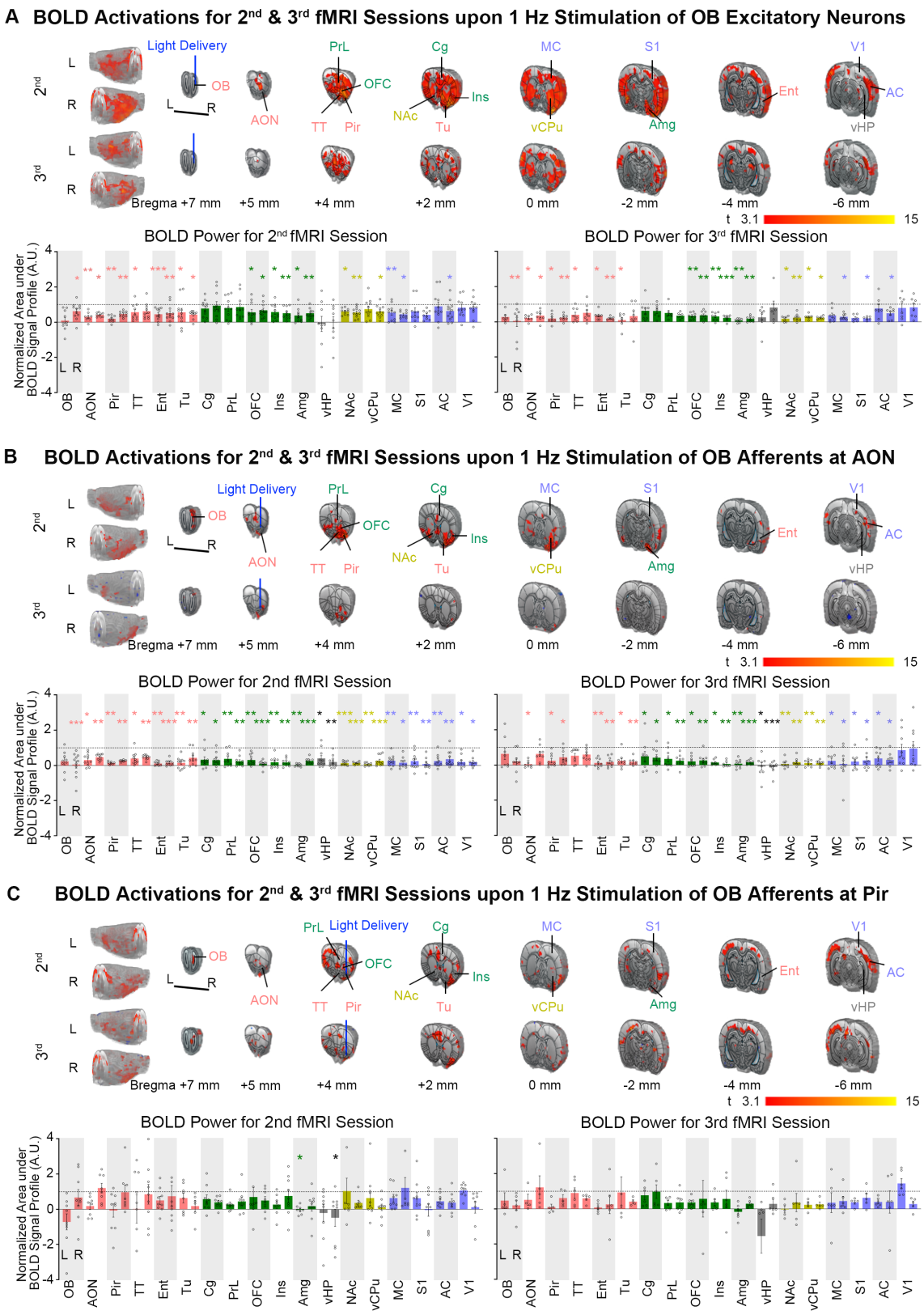


**Figure 3. Repetitive optogenetic excitation of OB excitatory neurons and OB afferents at AON and Pir reveal varied neural activity adaptation properties in olfactory networks.** Averaged BOLD activation maps (Top) upon 1 Hz stimulation of (**A**) OB excitatory neurons,

1038 (**B**) OB afferents in AON, and (**C**) OB afferents in Pir during the second (n = 11 for fMRI
1039 experiments in A & B; n = 9 for C; t > 3.1 corresponding to $P < 0.001$) and third (n = 8 for
1040 fMRI experiments in A; n = 9 for B; n = 6 for C; t > 3.1 corresponding to $P < 0.001$) fMRI
1041 sessions, respectively. We found a dramatic decrease or even absent bilateral activations in
1042 long-range olfactory networks upon stimulation of OB excitatory neurons or OB afferents at
1043 AON, but not Pir, indicating strong neural activity adaptation mediated by AON-driven neural
1044 activity to downstream targets. Note that similar to Fig. 2, the BOLD activation maps displayed
1045 in A-C were further corrected for multiple comparisons with threshold-free cluster
1046 enhancement with family-wise error rate (TFCE-FWE) at $P < 0.05$, except for that the maps
1047 during the third session in B and C were generated directly after one-sample t-test. The extent
1048 of neural activity adaptation in brain-wide olfactory networks was quantified with the true
1049 BOLD power (AUC of the BOLD signal profiles) for each atlas-defined ROI (Bottom;
1050 individual animal data points are shown; error bars indicate ± SEM; Dunnett's multiple
1051 comparisons test of BOLD power during 2$^{nd}$ vs. 1$^{st}$ fMRI session, 3$^{rd}$ vs. 1$^{st}$ session; ***$P <$
1052 $0.001$; **$P < 0.01$; *$P < 0.05$). Note that the AUC for each ROI was normalized to their
1053 respective counterpart in the first fMRI session for display.

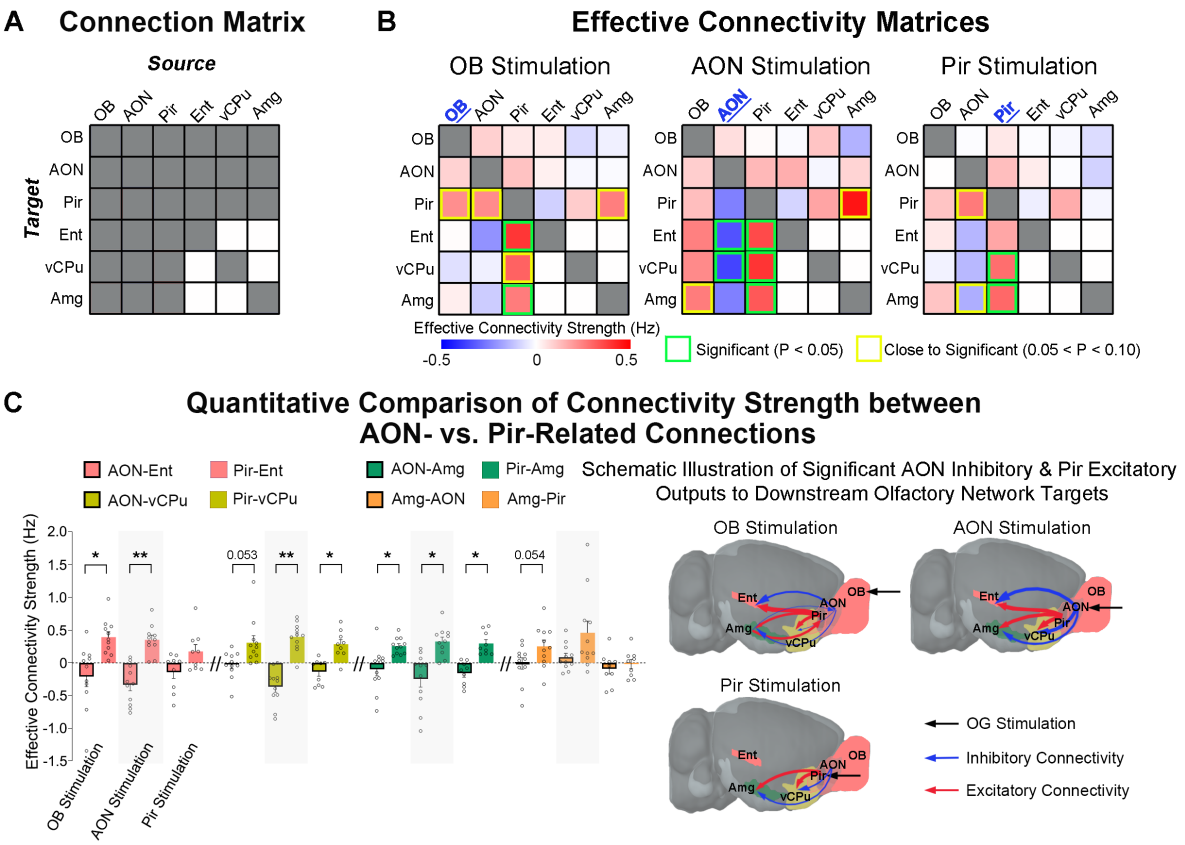


**Figure 4. Inhibitory effect of AON outputs and excitatory effect of Pir outputs to downstream targets in long-range olfactory networks.** (**A**) Graphical representation of matrix A which defines the a priori anatomical connections of the olfactory network model utilized in dynamic causal modeling (DCM). (**B**) Effective connectivity matrices of the olfactory network model upon stimulation of OB excitatory neurons and their afferents at AON and Pir. (**C**) Quantitative summary of the significant differences in connectivity strength of downstream connections identified from the statistical comparison of matrices in B (Left; n = 11 for OB and AON stimulations; n = 9 for Pir stimulation; individual animal data points are shown; error bars indicate ± SEM; paired t-test with FDR correction; $^{**}P < 0.01$, and $^{*}P < 0.05$) and the corresponding graphical representation of inhibitory effect of AON and excitatory effect of Pir outputs to downstream targets (Right). We identified robust AON negative vs. Pir positive connectivity to downstream targets such as Ent, vCPu and Amg, indicating distinct inhibitory vs. excitatory effect of the two primary olfactory cortical outputs that can shape the dynamic properties (i.e., BOLD activations across repeated stimulation sessions) of long-range olfactory networks.

1070

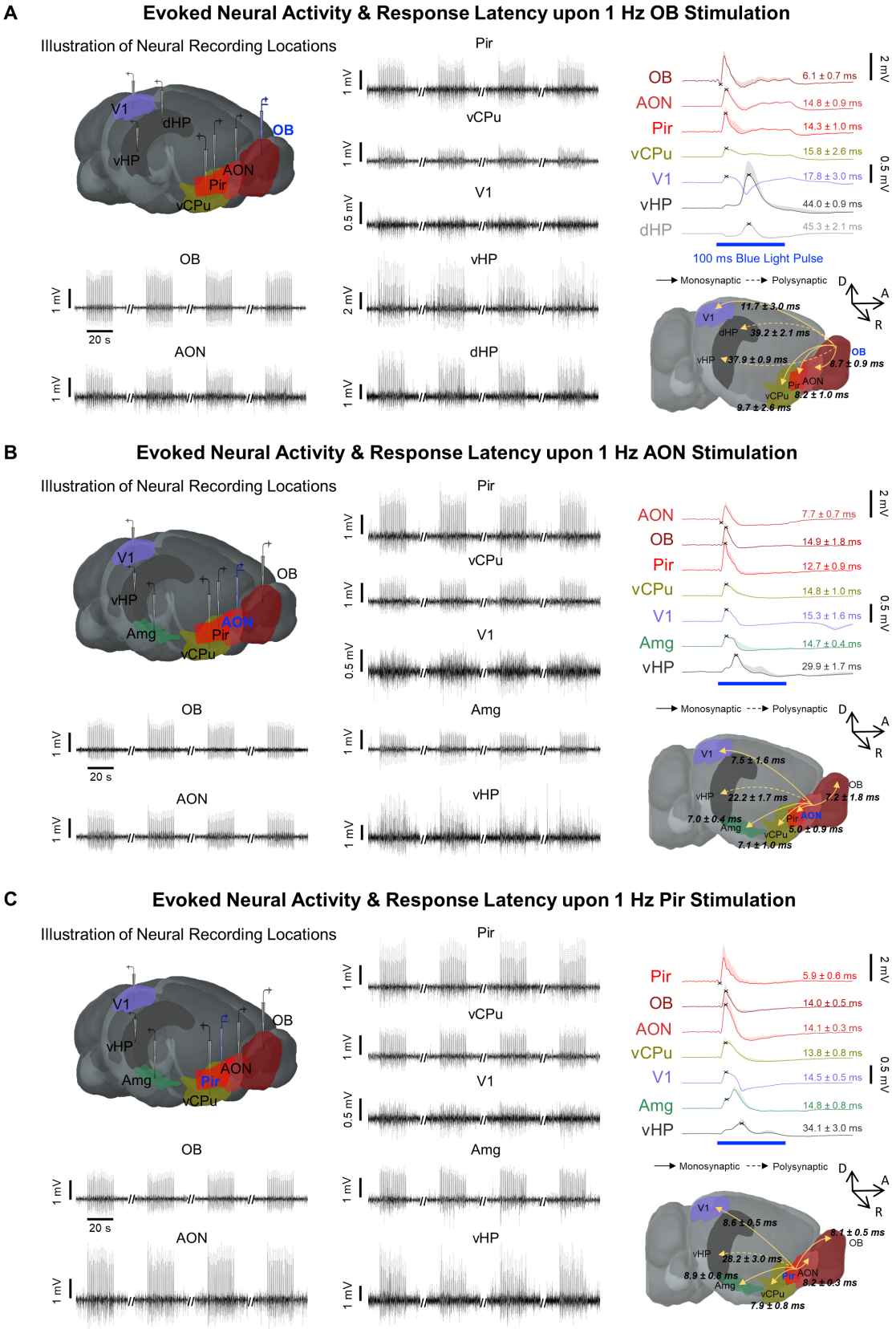


1071

1072 **Figure 5. Local field potential (LFP) recordings confirm neuronal activity underlying**

1073 **BOLD activations and reveal orthodromic neural activity propagation to downstream**

**targets in primary olfactory, striatal, visual, limbic and hippocampal networks.** Illustration of electrophysiological recording regions (Top-Left), averaged evoked LFPs from the seven recorded regions (Bottom-Left & Middle), and summary of orthodromic neural activity propagation latencies measured from the stimulation onset over mono- and poly-synaptic projections (Right) upon 1 Hz optogenetic stimulation of (**A**) OB excitatory neurons, (**B**) OB afferents at AON and (**C**) OB afferents at Pir (n = 7, n = 7 and n = 5, respectively; 10% duty cycle; error bars indicate ± SEM; crosshairs denote LFP peaks that represent initial neuronal population activity for latency measurements). Significant delay between AON/Pir and OB neuronal population activity with appreciable jitter showed that neural activity propagation through the excitations of OB axonal terminals at AON or Pir, respectively, were largely orthodromic in our experiment.

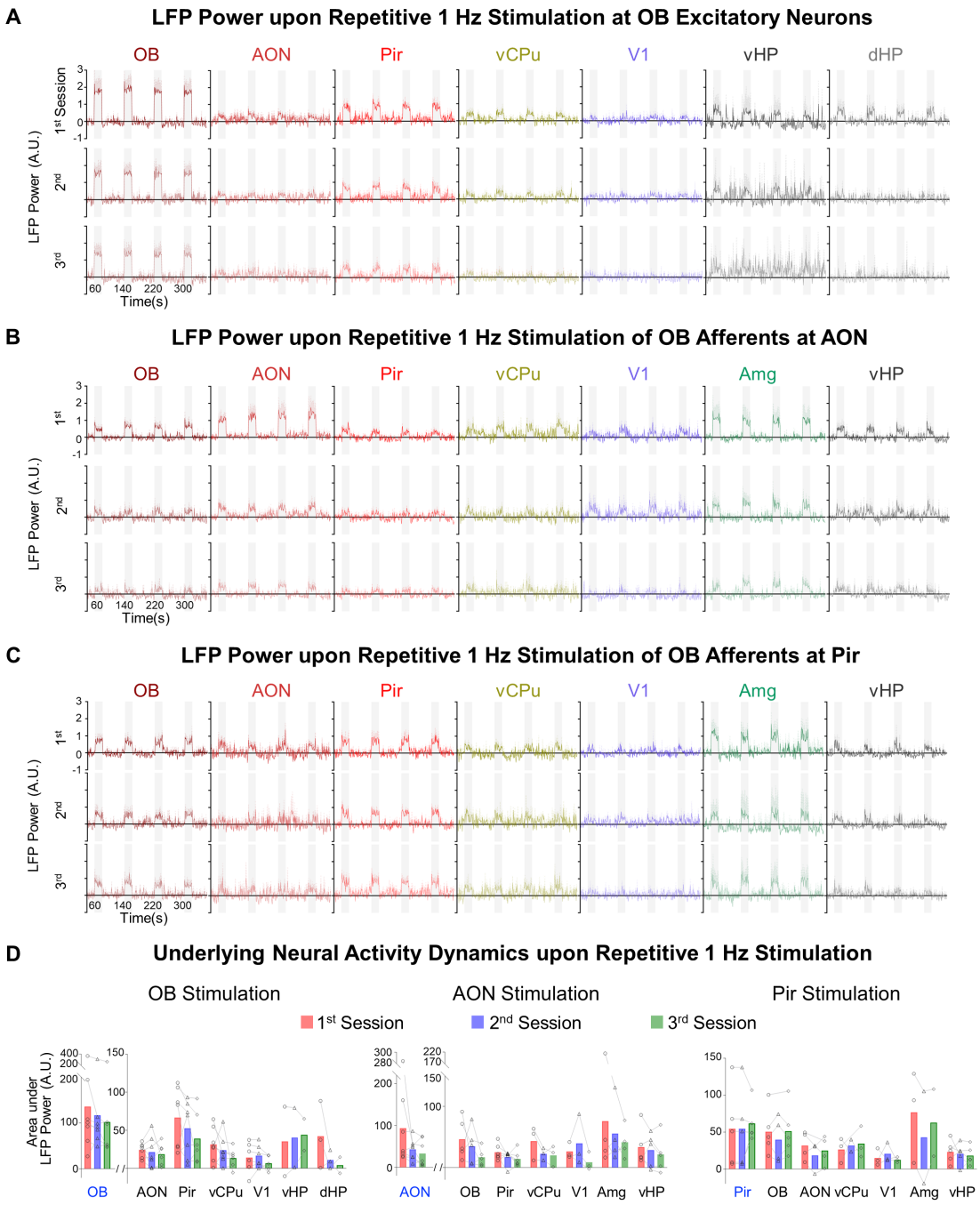


**Figure 6. LFP recordings confirm varied neural activity adaptation in olfactory networks upon repetitive optogenetic excitations of OB excitatory neurons and OB afferents at AON and Pir.** LFP power of evoked neural activities upon 1 Hz optogenetic stimulation of (**A**) OB excitatory neurons (n = 7; 10% duty cycle; error bars indicate ± SEM), (**B**) OB afferents at AON (n = 7; 10% duty cycle; error bars indicate ± SEM) and (**C**) OB afferents at Pir (n = 5; 10% duty cycle; error bars indicate ± SEM) across three electrophysiological recordings sessions. (**D**) Summary of the area under LFP power to quantify the extent of neural activity adaptation in the recorded regions of olfactory networks (individual animal data points are

shown). In accord with our fMRI findings, the strength of neural activities, which were quantified through LFP power analysis here (i.e., area under absolute LFP trace normalized to 30-s baseline LFP power), was also decreased under repetitive 1 Hz stimulation of OB and OB afferents at AON but was relatively unchanged under Pir stimulation (1st vs 2nd and 3rd recording sessions). The LFP recordings demonstrate strong neural activity adaptation mediated by AON-driven neural activities to downstream targets.

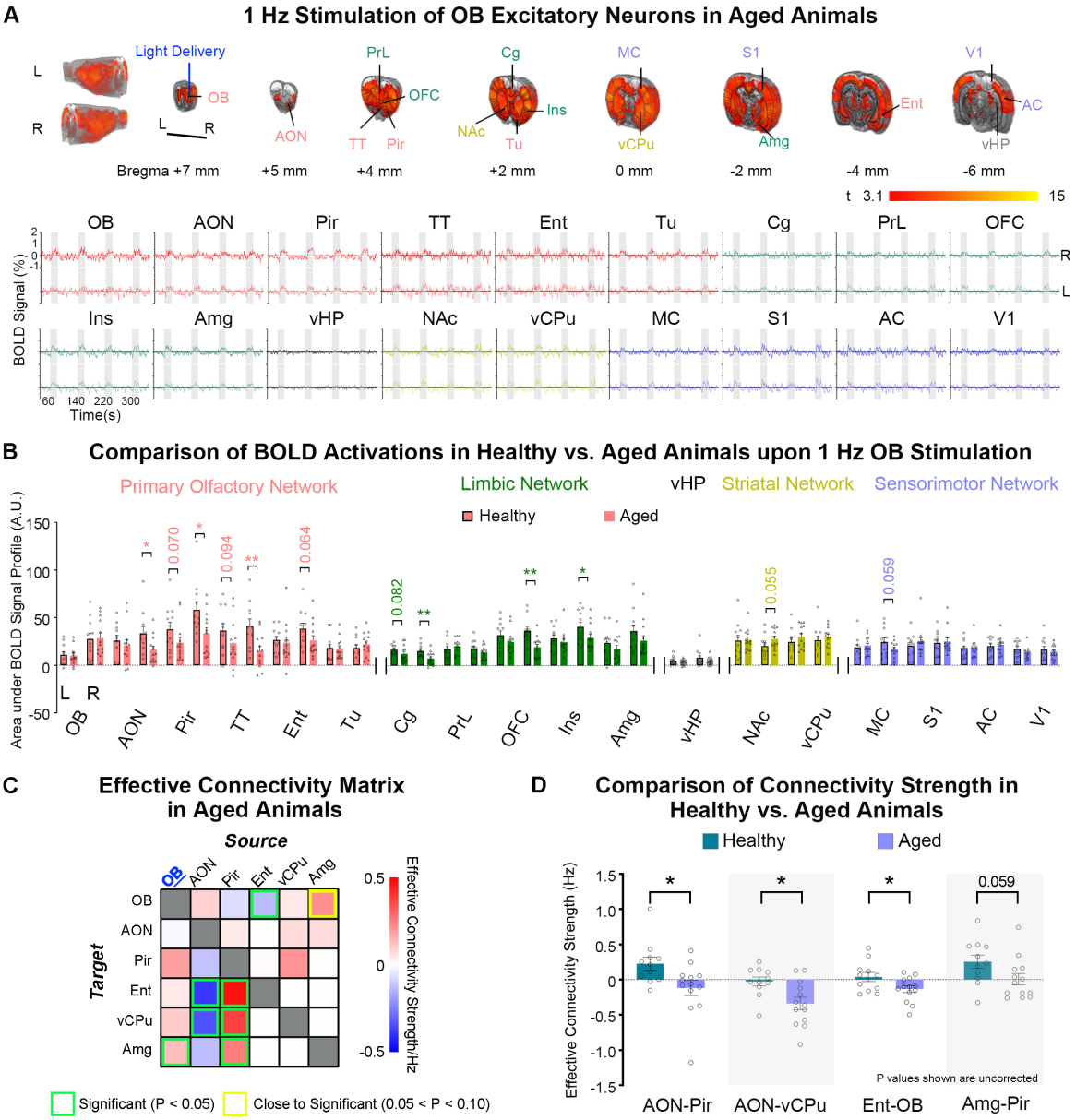


**Figure 7. Decreased BOLD activations in primary olfactory and limbic networks, and impaired AON to Pir connectivity in aged animals. (A)** Averaged BOLD activation maps and signal profiles from the 1st fMRI session upon 1 Hz stimulation of OB excitatory neurons in D-galactose aged rat model (n = 13; t > 3.1 corresponding to $P < 0.001$; error bars indicate ± SEM). Note that the BOLD activation maps displayed in A were further corrected for multiple comparisons with TFCE-FWE at $P < 0.05$. (**B**) Comparison of the corresponding area under the BOLD signal profiles for each atlas-defined region-of-interests between healthy and aged animals (individual animal data points are shown; Fisher's LSD test; $^{**}P < 0.01$, and $^{*}P < 0.05$; error bars indicate ± SEM). (**C**) Effective connectivity matrices of the olfactory network model upon stimulation of OB excitatory neurons in aged brains. (**D**) Quantitative summary of

the significant differences in connectivity strength of downstream connections identified from the statistical comparison of effective connectivity matrices between healthy and aged brains (individual animal data points are shown; unpaired t-test; $*P < 0.05$; error bars indicate ± SEM). We uncovered a switch in the polarity from positive to negative in the connectivity of AON neural activity outputs to Pir in aged animals, indicating the dysfunction of a key primary olfactory cortical circuit that likely caused the significantly decreased BOLD activations in the primary olfactory and limbic networks.

## A Immunohistochemistry of CaMKIIα::ChR2(H1234R) Viral Expression in OB, AON & Pir

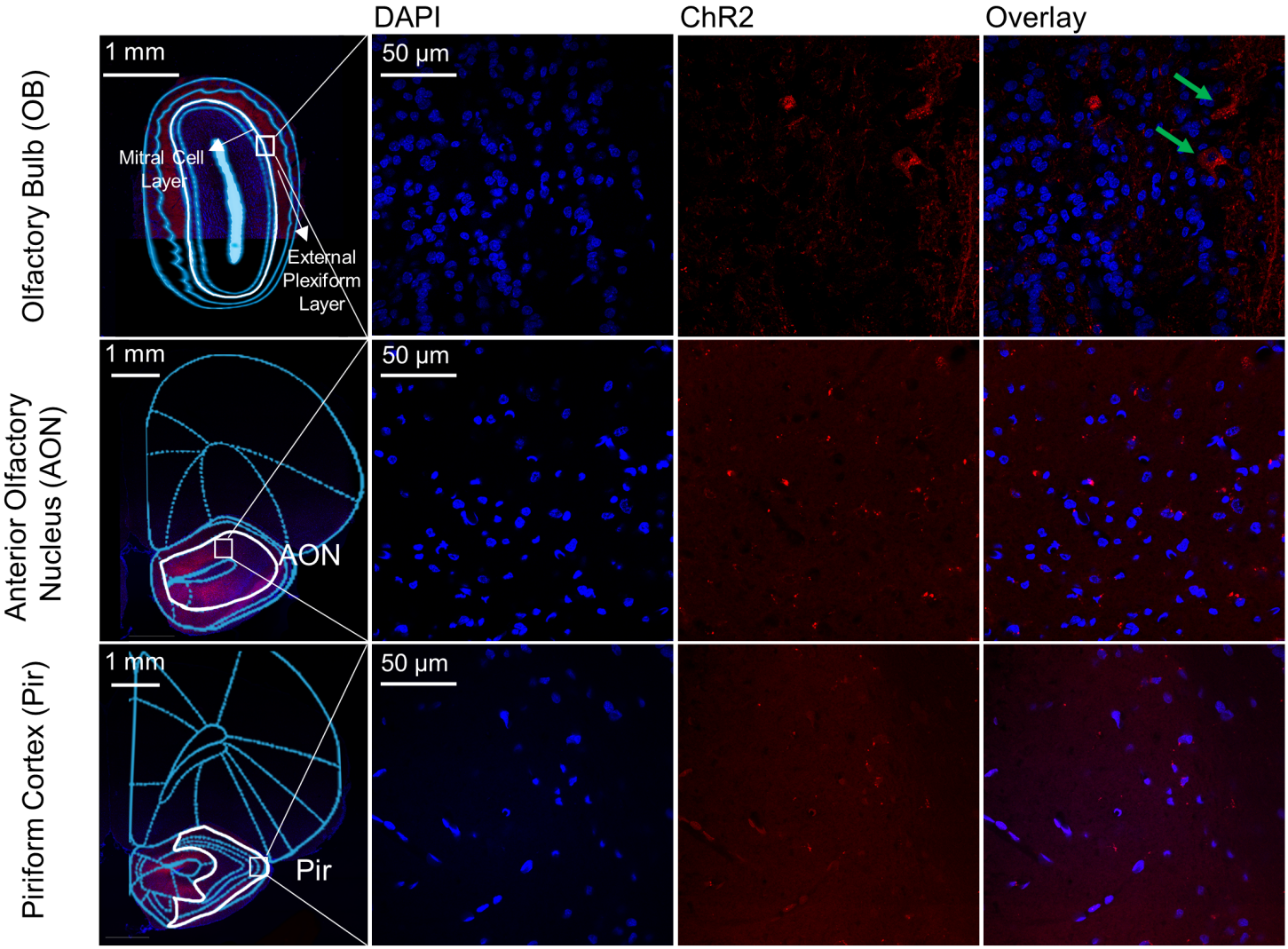


## B Illustration of Optogenetic fMRI Stimulation Setup and Paradigm

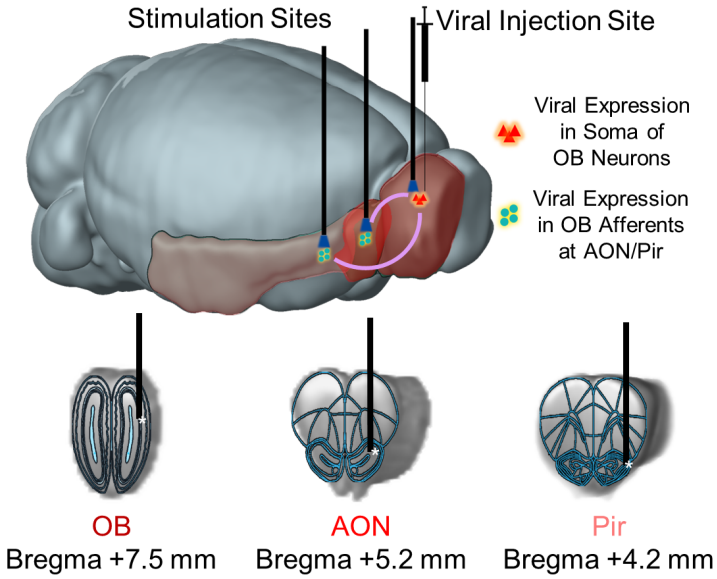


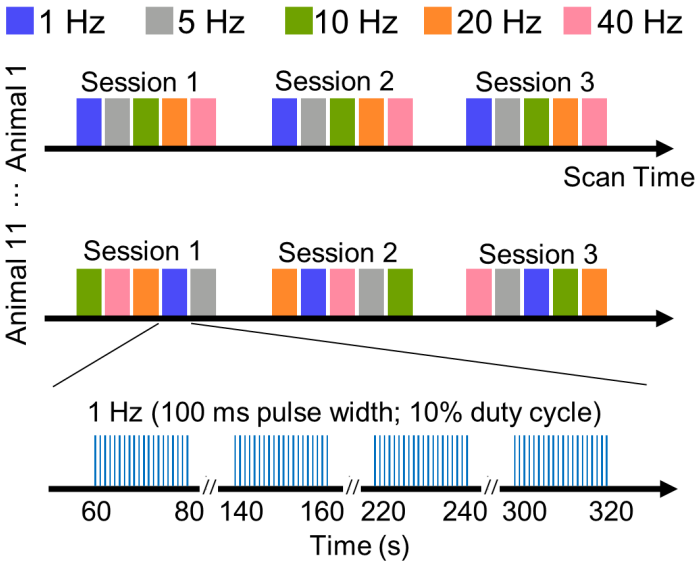

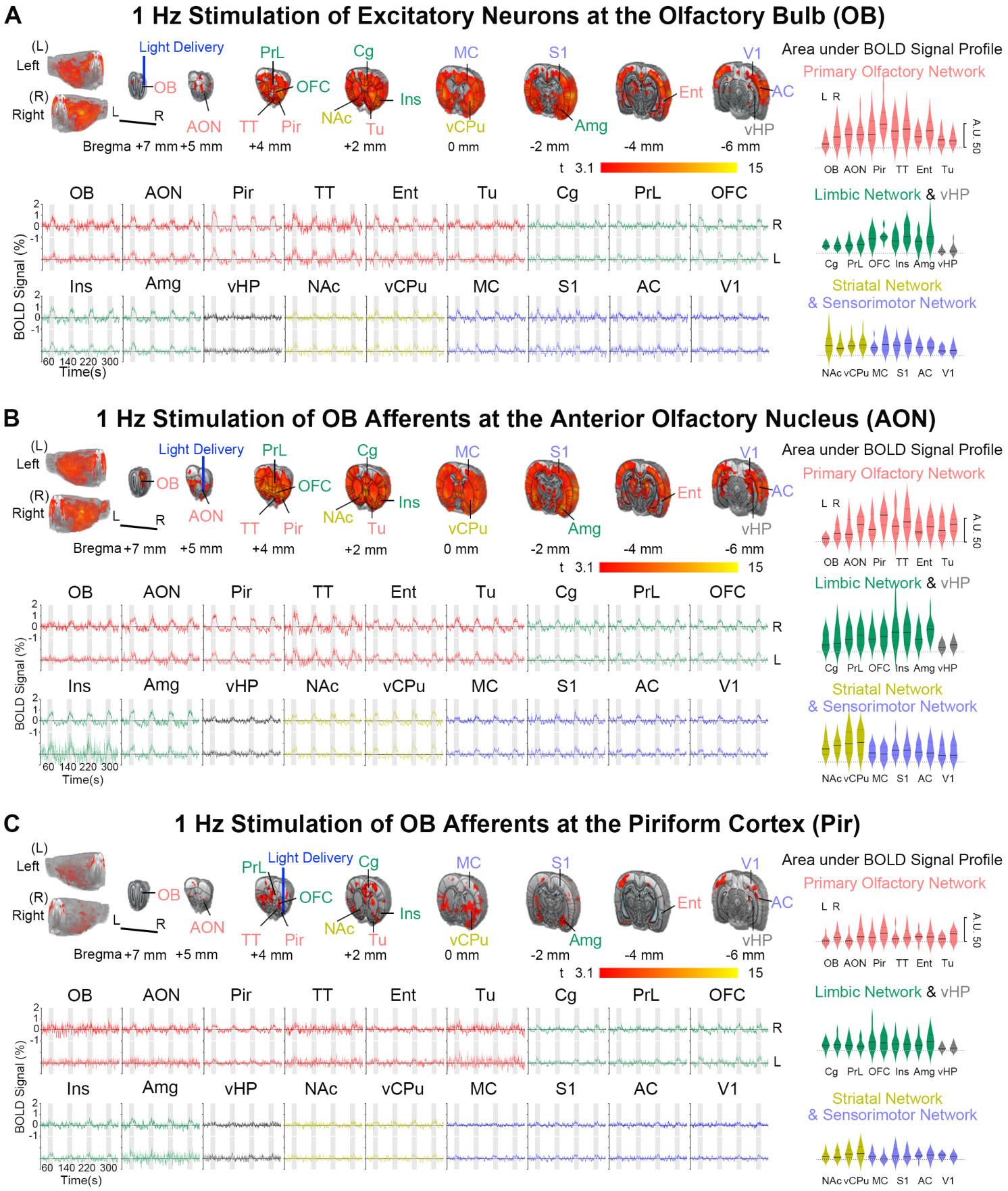
A
1 Hz Stimulation of Excitatory Neurons at the Olfactory Bulb (OB)
B
1 Hz Stimulation of OB Afferents at the Anterior Olfactory Nucleus (AON)
C
1 Hz Stimulation of OB Afferents at the Piriform Cortex (Pir)
(L) Left
(R) Right
Light Delivery
OB
AON
PrL
OFC
TT
Pir
Cg
NAc
Tu
Ins
MC
vCPu
S1
Amg
Ent
V1
AC
vHP
Bregma +7 mm +5 mm +4 mm +2 mm 0 mm -2 mm -4 mm -6 mm
t 3.1 15
Area under BOLD Signal Profile
Primary Olfactory Network
Limbic Network & vHP
Striatal Network & Sensorimotor Network
BOLD Signal (%)
Time(s)
60 140 220 300
A.U. 50
D
BOLD Activation Strength Across Various Networks upon Stimulation of Distinct Olfactory Targets
OB Stimulation
AON Stimulation
Pir Stimulation
BOLD Activation Strength (%)
0.07

## A BOLD Activations for 2nd & 3rd fMRI Sessions upon 1 Hz Stimulation of OB Excitatory Neurons

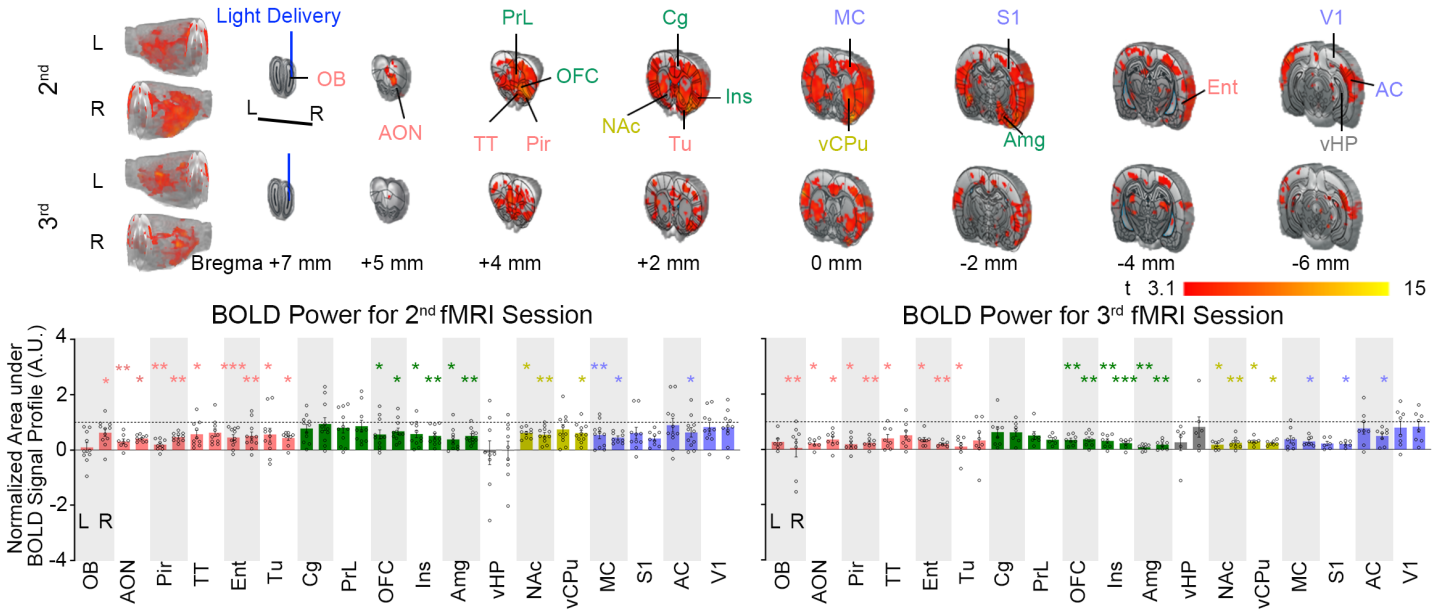


## B BOLD Activations for 2nd & 3rd fMRI Sessions upon 1 Hz Stimulation of OB Afferents at AON

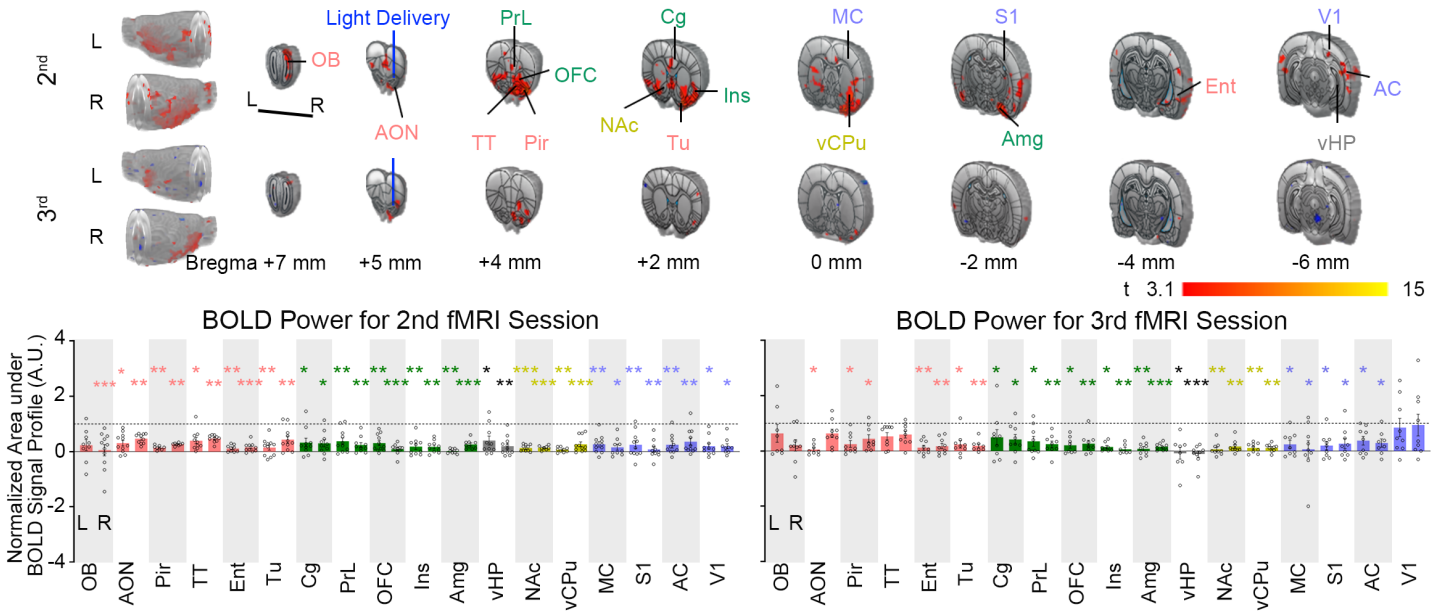


## C BOLD Activations for 2nd & 3rd fMRI Sessions upon 1 Hz Stimulation of OB Afferents at Pir

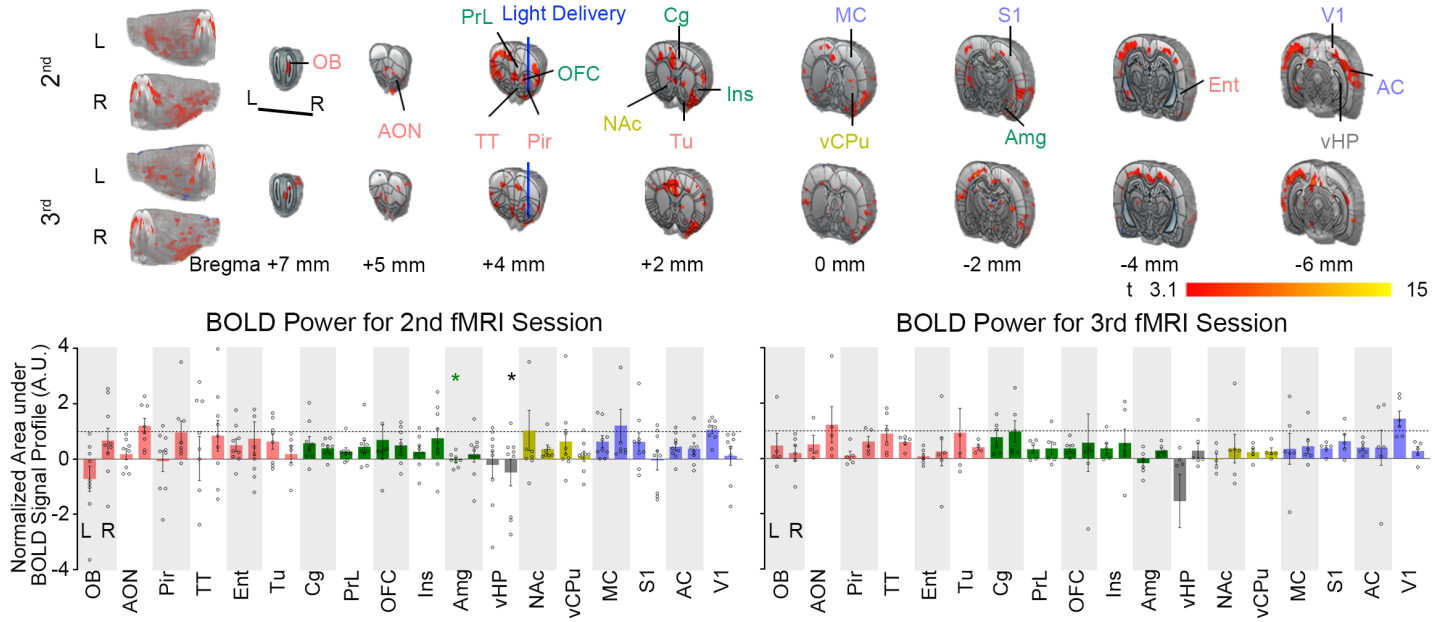

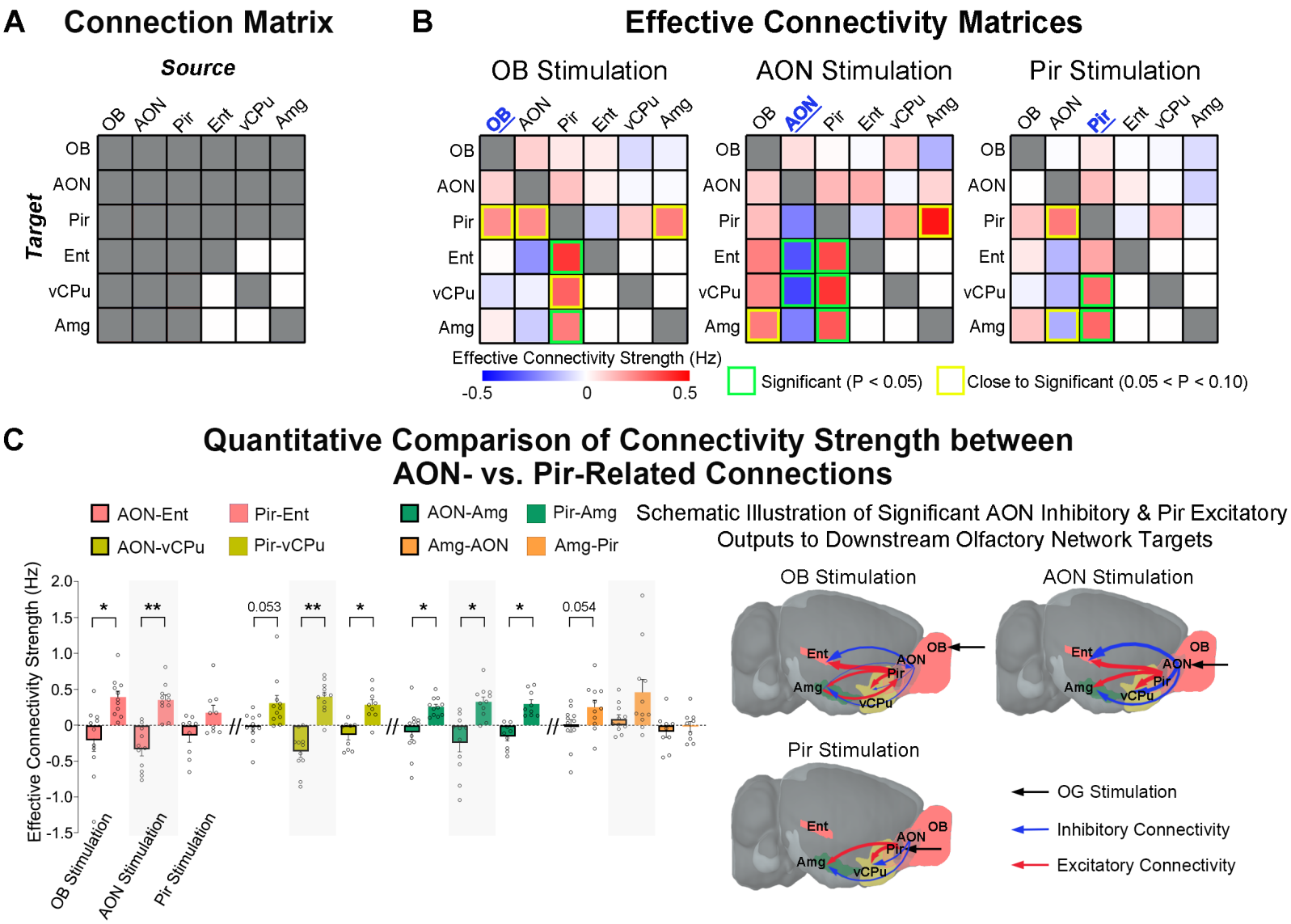
A
Connection Matrix
Source
Target
OB
AON
Pir
Ent
vCPu
Amg
B
Effective Connectivity Matrices
OB Stimulation
AON Stimulation
Pir Stimulation
Effective Connectivity Strength (Hz)
-0.5
0
0.5
Significant (P < 0.05)
Close to Significant (0.05 < P < 0.10)
C
Quantitative Comparison of Connectivity Strength between AON- vs. Pir-Related Connections
AON-Ent
Pir-Ent
AON-vCPu
Pir-vCPu
AON-Amg
Pir-Amg
Amg-AON
Amg-Pir
Effective Connectivity Strength (Hz)
2.0
1.5
1.0
0.5
0
-0.5
-1.0
-1.5
*
**
0.053
0.054
OB Stimulation
AON Stimulation
Pir Stimulation
Schematic Illustration of Significant AON Inhibitory & Pir Excitatory Outputs to Downstream Olfactory Network Targets
OB Stimulation
AON Stimulation
Pir Stimulation
Ent
OB
AON
Pir
Amg
vCPu
OG Stimulation
Inhibitory Connectivity
Excitatory Connectivity

## A Evoked Neural Activity & Response Latency upon 1 Hz OB Stimulation

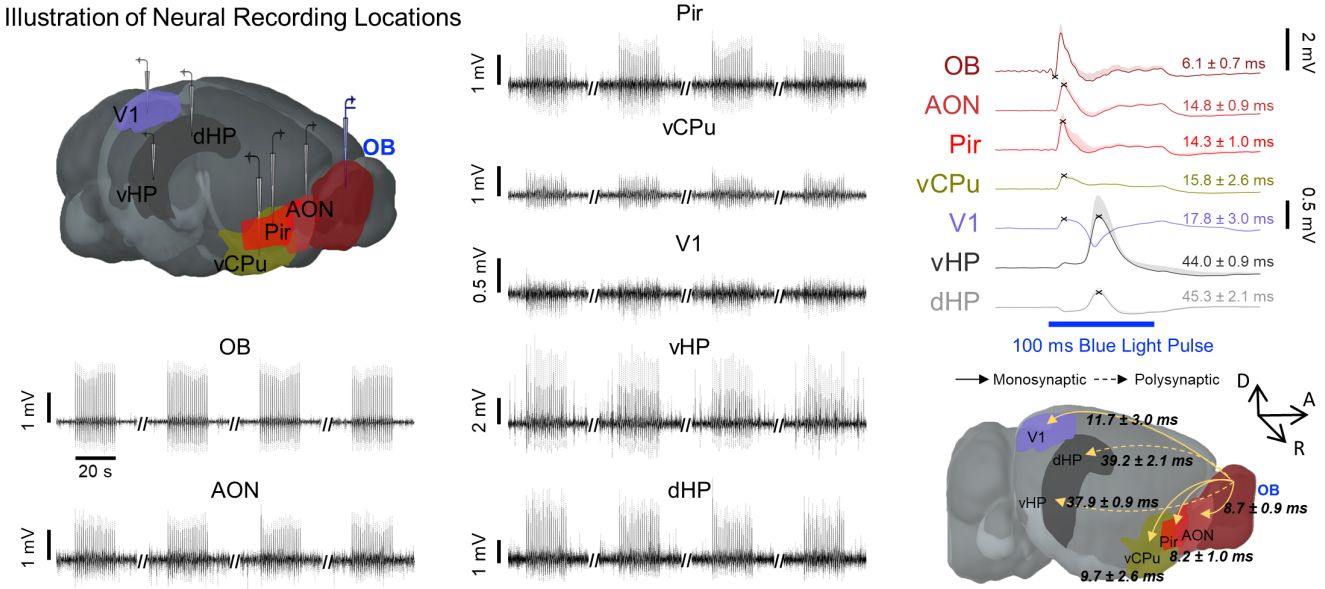


## B Evoked Neural Activity & Response Latency upon 1 Hz AON Stimulation

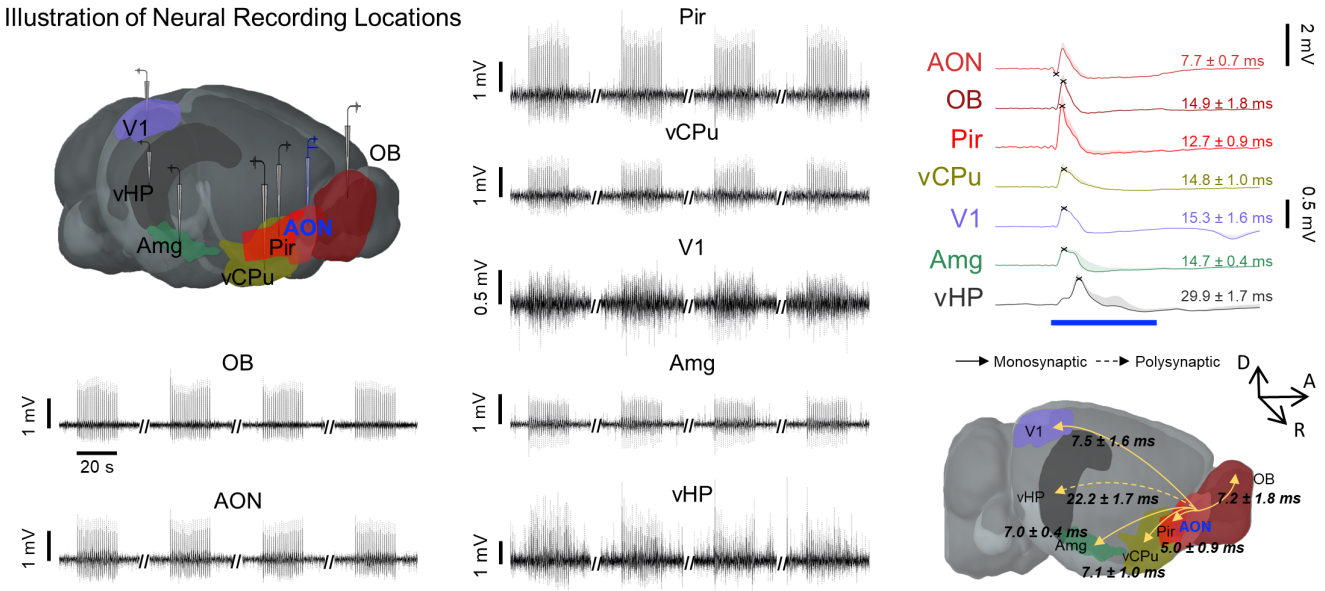


## C Evoked Neural Activity & Response Latency upon 1 Hz Pir Stimulation

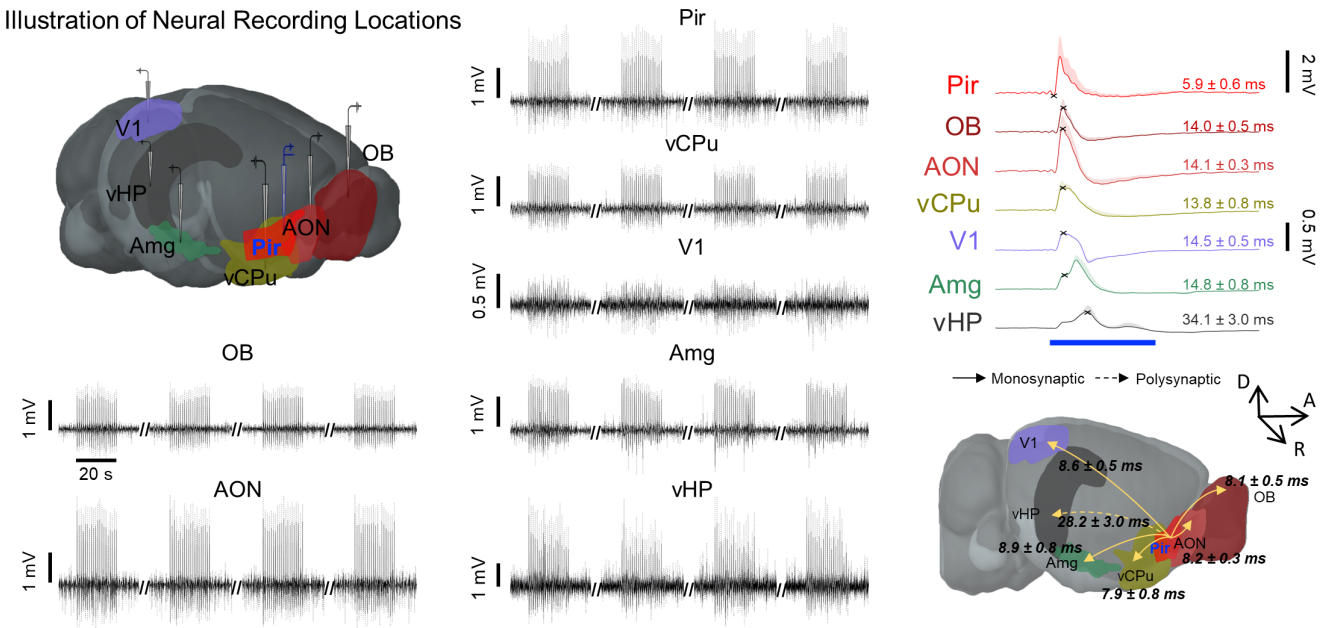

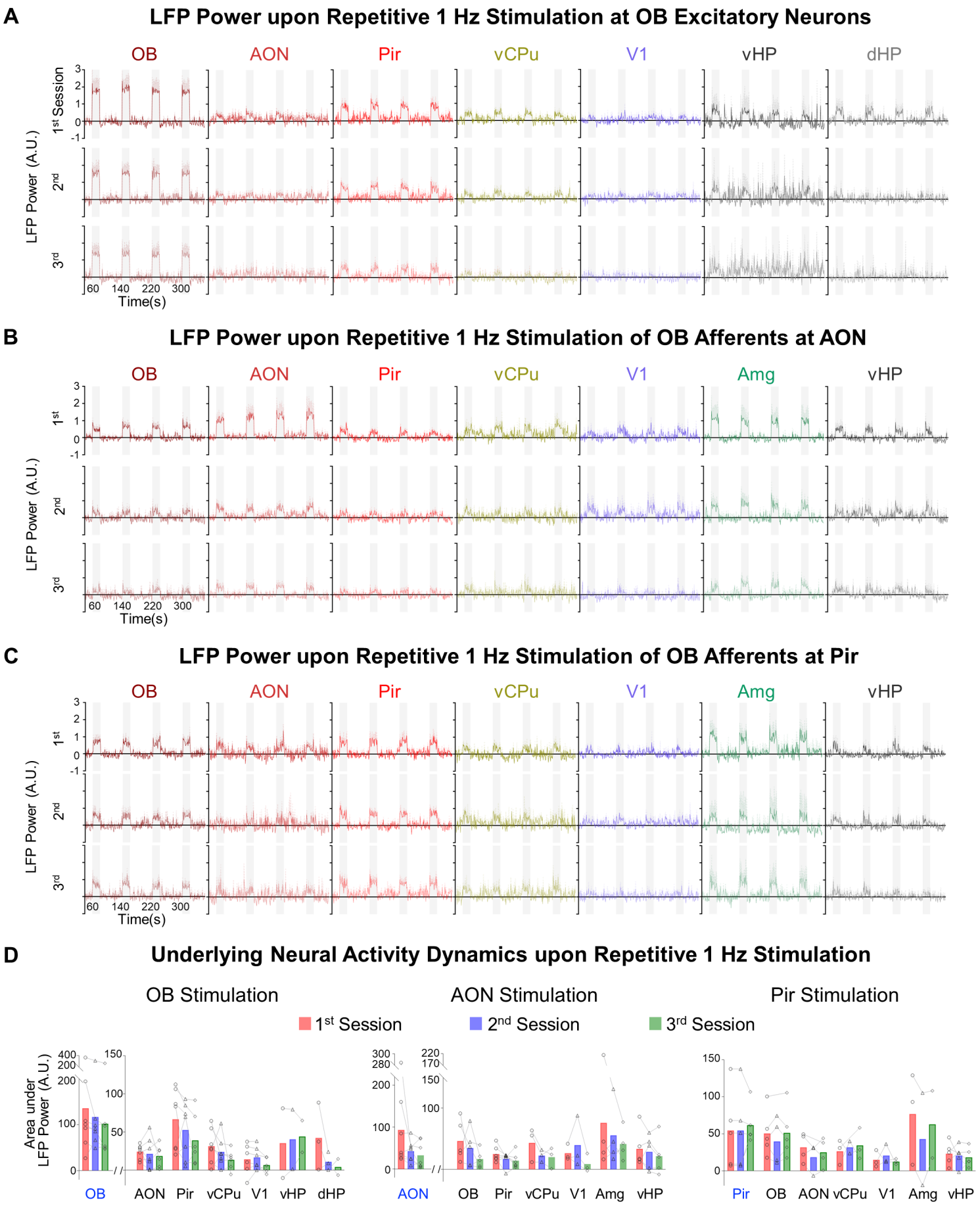
A
LFP Power upon Repetitive 1 Hz Stimulation at OB Excitatory Neurons
OB
AON
Pir
vCPu
V1
vHP
dHP
1st Session
2nd
3rd
LFP Power (A.U.)
Time(s)
B
LFP Power upon Repetitive 1 Hz Stimulation of OB Afferents at AON
Amg
C
LFP Power upon Repetitive 1 Hz Stimulation of OB Afferents at Pir
D
Underlying Neural Activity Dynamics upon Repetitive 1 Hz Stimulation
OB Stimulation
AON Stimulation
Pir Stimulation
1st Session
2nd Session
3rd Session
Area under LFP Power (A.U.)

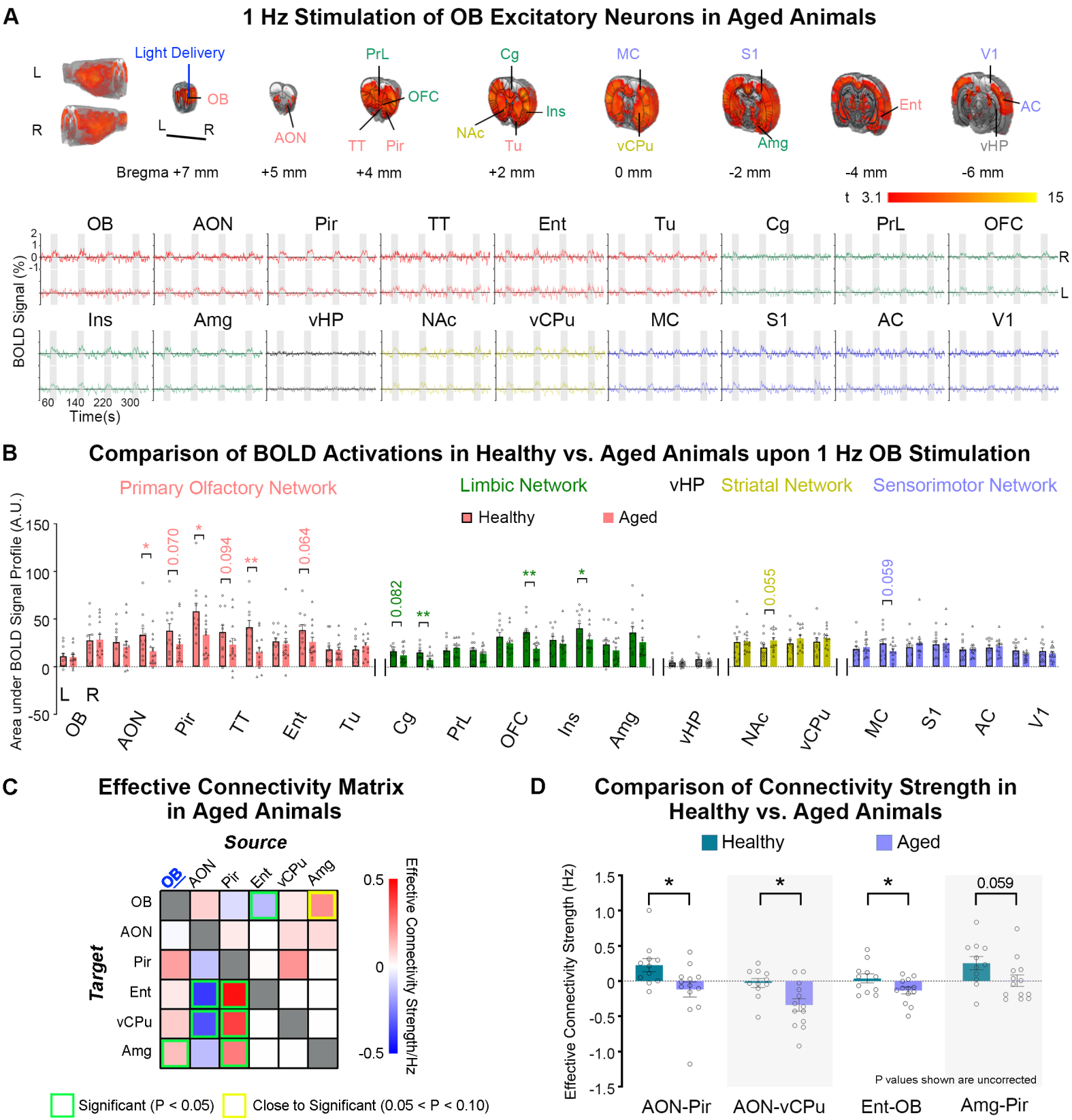
A
1 Hz Stimulation of OB Excitatory Neurons in Aged Animals
Light Delivery
L
R
OB
AON
PrL
OFC
TT
Pir
Cg
Ins
NAc
Tu
MC
vCPu
S1
Amg
Ent
V1
AC
vHP
Bregma +7 mm
+5 mm
+4 mm
+2 mm
0 mm
-2 mm
-4 mm
-6 mm
t 3.1
15
OB
AON
Pir
TT
Ent
Tu
Cg
PrL
OFC
Ins
Amg
vHP
NAc
vCPu
MC
S1
AC
V1
BOLD Signal (%)
Time(s)
B
Comparison of BOLD Activations in Healthy vs. Aged Animals upon 1 Hz OB Stimulation
Primary Olfactory Network
Limbic Network
vHP
Striatal Network
Sensorimotor Network
Healthy
Aged
Area under BOLD Signal Profile (A.U.)
0.070
0.094
0.064
0.082
0.055
0.059
C
Effective Connectivity Matrix in Aged Animals
Source
Target
Effective Connectivity Strength/Hz
Significant (P < 0.05)
Close to Significant (0.05 < P < 0.10)
D
Comparison of Connectivity Strength in Healthy vs. Aged Animals
Healthy
Aged
Effective Connectivity Strength (Hz)
0.059
P values shown are uncorrected
AON-Pir
AON-vCPu
Ent-OB
Amg-Pir